# Coversheet for "Intraseasonal Sea-Level Variability in the Persian Gulf"

Christopher G. Piecuch[1,†], Ichiro Fukumori[2,‡], & Rui M. Ponte[3,*]

[1] *Woods Hole Oceanographic Institution, Woods Hole, Massachusetts, USA*

[2] *Jet Propulsion Laboratory, Pasadena, California, USA*

[3] *Atmospheric and Environmental Research, Inc., Lexington, Massachusetts, USA*



† cpiecuch@whoi.edu

‡ ichiro.fukumori@jpl.nasa.gov

∗ rponte@aer.com

# Intraseasonal Sea-Level Variability in the Persian Gulf

Christopher G. Piecuch*

*Woods Hole Oceanographic Institution, Woods Hole, Massachusetts, USA*

Ichiro Fukumori

*Jet Propulsion Laboratory, Pasadena, California, USA*

Rui M. Ponte

*Atmospheric and Environmental Research, Inc., Lexington, Massachusetts, USA*

**Corresponding author*: Christopher G. Piecuch, cpiecuch@whoi.edu

ABSTRACT

Satellite observations are used to establish the dominant magnitudes, scales, and mechanisms of intraseasonal variability in ocean dynamic sea level ($\zeta$) in the Persian Gulf over 2002–2015. Empirical orthogonal function (EOF) analysis applied to altimetry data reveals a basin-wide, single-signed intraseasonal fluctuation that contributes importantly to $\zeta$ variance in the Persian Gulf at monthly to decadal timescales. An EOF analysis of Gravity Recovery and Climate Experiment (GRACE) observations over the same period returns a similar large-scale mode of intraseasonal variability, suggesting that the basin-wide intraseasonal $\zeta$ variation has a predominantly barotropic nature. A linear barotropic theory is developed to interpret the data. The theory represents Persian-Gulf-average $\zeta$ ($\overline{\zeta}$) in terms of local freshwater flux, barometric pressure, and wind stress forcing, as well as $\zeta$ at the boundary in the Gulf of Oman. The theory is tested using a multiple linear regression with these freshwater flux, barometric pressure, wind stress, and boundary $\zeta$ quantities as input, and $\overline{\zeta}$ as output. The regression explains $70\% \pm 9\%$ (95% confidence interval) of the intraseasonal $\overline{\zeta}$ variance. Numerical values of regression coefficients computed empirically from the data are consistent with theoretical expectations from first principles. Results point to a substantial non-isostatic response to surface loading. The Gulf of Oman $\zeta$ boundary condition shows lagged correlation with $\zeta$ upstream along the Indian Subcontinent, Maritime Continent, and equatorial Indian Ocean, suggesting a large-scale Indian-Ocean influence on intraseasonal $\overline{\zeta}$ variation mediated by coastal and equatorial waves, and hinting at potential predictability. This study highlights the value of GRACE for understanding sea level in an understudied marginal sea.

## 1. Introduction

The Persian Gulf[1] is a semi-enclosed marginal sea of the Indian Ocean (Figure 1). It connects to the Arabian Sea to the southeast through the Strait of Hormuz and the Gulf of Oman. The Persian Gulf is shallow and broad, with an average depth of $\sim 30$ m and a surface area of $\sim 2.2 \times 10^5$ km$^2$. It is subject to an arid, subtropical climate, and is bounded to the southwest by the Arabian Desert and by the Zagros mountains to the northeast.

Past studies establish the basic physical oceanography of the Persian Gulf using data and models (Chao et al., 1992; Emery, 1956; Johns et al., 1999, 2003; Kämpf and Sadrinasab, 2006; Reynolds, 1993; Thoppil and Hogan, 2010; Swift and Bower, 2003; Yao and Johns, 2010). We outline some of the salient features for context. The region is forced year-round by north-northwesterly surface winds ('shamal', speeds 3–6 m s$^{-1}$). Evaporation ($\sim 2$ m y$^{-1}$) far exceeds precipitation and runoff ($\sim 0.2$ m y$^{-1}$), resulting in an inverse-estuarine circulation—fresher, warmer buoyant waters inflow near the surface through the Strait of Hormuz largely along the coast of Iran, whereas saltier, colder, denser waters outflow near the bottom mainly along the coast of the United Arab Emirates. The basin-scale circulation is demarcated by a thermal front across the Persian Gulf between Qatar and Iran. Northwest of the front, there is equatorward flow along Saudi Arabia driven by wind-forced downwelling at the coast and buoyant river discharge from the Tigris, Euphrates, and other rivers at the head of the Persian Gulf. To the southeast, there exists a large-scale counterclockwise circulation, maintained by exchanges through the Strait of Hormuz, and evaporation, cooling, and sinking of water masses in shallow regions along the southern Persian Gulf. Mesoscale eddies are common, especially during boreal summer, when they are shed from the Iranian Coastal Jet due to baroclinic instability. There is a seasonal cycle in the vertical stratification, such that top-to-bottom

[1]The name of this body of water is subject to dispute. It is also known as the Arabian Gulf or the Gulf. We use the name Persian Gulf following the conventions of the International Hydrographic Organization and the United Nations.

potential density contrasts are weaker in winter (0–1 kg $m^{-3}$) and stronger in summer (2–5 kg $m^{-3}$). For more details, interested readers are directed to the papers cited above.

The Persian Gulf is one of the world ocean's busiest waterways, due to its vast oil and gas stores, which are of longstanding geopolitical, economic, and military interest (al-Chalabi, 2007; Barnes and Myers Jaffe, 2006; Larson, 2007). Bordering eight nations, the Persian Gulf is also home to large coastal populations and major coastal cities including Dubai, Abu Dhabi, and Doha, which are exposed to risk of flooding and inundation related to sea-level change (Al-Jeneid et al., 2008; Lafta et al., 2020). Kopp et al. (2014, 2017) project that mean sea level will rise by 44–108 cm between 2000 and 2100 in Bahrain under the Representative Concentration Pathway 8.5 forcing scenario (66% confidence). This would threaten ~ 10–15% (~ 80–100 $km^2$) of Bahrain's surface area (Al-Jeneid et al., 2008). Such numbers emphasize the importance of understanding sea-level changes in the Persian Gulf. However, projections of mean sea-level rise on multidecadal and longer timescales (Kopp et al., 2014, 2017) alone are insufficient to anticipate future coastal flood risk. Also important are sea-level fluctuations at decadal and shorter periods, which can superimpose on longer-term changes, temporarily ameliorating or exacerbating coastal risk (Burgos et al., 2018; Dangendorf et al., 2016; Long et al., 2020; Ray and Foster, 2016; Sweet et al., 2017). This motivates a detailed investigation of mean sea-level variation in the Persian Gulf on decadal and shorter timescales—what are the dominant magnitudes, scales, and mechanisms?

Past studies on Persian Gulf mean sea level largely focus on seasonal cycles and decadal trends (Al-Subhi, 2010; Alothman et al., 2014; Ayhan, 2020; Barzandeh et al., 2018; El-Gindy, 1991; El-Gindy and Eid, 1997; Hassanzadeh et al., 2007; Hosseinibalam et al., 2007; Sharaf El Din, 1990; Siddig et al., 2019; Sultan et al., 1995a, 2000). Sultan et al. (1995a) consider monthly relative sea level during 1980–1990 from two tide gauges on the Saudi Arabia coast. They find that 80% of the overall monthly data variance is explained by the seasonal cycle, which has an amplitude of ~ 10 cm and peaks in boreal summer. These authors argue that 75% of the seasonal variance in sea level reflects an inverted-barometer response to a ~ 10-mb-amplitude seasonal cycle in local surface air pressure, and that the remaining 25% of seasonal variance represents steric variability owing to density fluctuations. Other studies targeting different regions, tide gauges, and time periods confirm this basic result that inverted-barometer and steric effects make primary and secondary contributions, respectively, to the large-scale seasonal cycle in Persian Gulf sea level, but also suggest that local wind effects are important in some places (Al-Subhi, 2010; Barzandeh et al., 2018; El-Gindy, 1991; El-Gindy and Eid, 1997; Hassanzadeh et al., 2007; Hosseinibalam et al., 2007; Sharaf El Din, 1990; Sultan et al., 2000). Alothman et al. (2014) interrogate monthly relative sea level over 1979–2007 based on 15 tide-gauge records from Bahrain, Saudi Arabia, and Iran, along with measurements of vertical land motion from 6 Global Positioning System (GPS) stations in Bahrain, Saudi Arabia, and Kuwait. They determine that regional relative sea level rose by $2.2 \pm 0.5$ mm $y^{-1}$ over that time. These authors find that one-third of the increase ($0.7 \pm 0.6$ mm $y^{-1}$) was due to crustal subsidence, possibly related to groundwater pumping and oil extraction (Amin and Bankher, 1997), and the remaining two-thirds ($1.5 \pm 0.8$ mm $y^{-1}$) was due to geocentric sea-level changes. Sultan et al. (2000) calculate a more muted relative sea-level trend (1.7 mm $y^{-1}$) based on 9 tide-gauge records from Saudi Arabia over 1980–1994, while Siddig et al. (2019) estimate a larger geocentric sea-level trend ($3.6 \pm 0.4$ mm $y^{-1}$) from altimetry data averaged over the Persian Gulf during 1993–2018, consistent with reports of a global sea-level acceleration in recent decades (Nerem et al., 2018; Dangendorf et al., 2019; Frederikse et al., 2020).

Omitted from past works on Persian Gulf mean sea level is exploration of nonseasonal sea-level variation. This is an important omission, since nonseasonal variations in general, and in particular intraseasonal variations, contribute importantly to mean sea-level variance over the Persian Gulf on monthly to decadal timescales. For example, consider the time series of monthly ocean dynamic sea level[2] from satellite-altimetry data averaged over the Persian Gulf during 2002–2015 shown in Figure 2. Filters are applied to the data to emphasize variability on different timescales, and global-mean sea level and the inverted-barometer effect are removed. Nonseasonal fluctuations explain 52% of the monthly data variance, and intraseasonal fluctuations (with ~ 2–6-month periods) alone account for 46% of the overall data variance. The altimetric time series of intraseasonal sea level averaged over the Persian Gulf also explains 51% of the intraseasonal variance in relative sea level averaged across 5 tide gauges from Iran and Bahrain during the overlapping period 2002–2006 (Figure 2). This exploratory analysis suggests that large-scale intraseasonal fluctuations make important contributions to ocean dynamic sea-level variance across the Persian Gulf during the altimeter era, motivating a more in-depth investigation.

Here we investigate the magnitudes, scales, and mechanisms of intraseasonal sea-level variability in the Persian Gulf through an analysis of satellite observations, tide gauges, reanalysis products, and gridded surface flux estimates. The remainder of the paper is structured as follows: in section 2, we describe the data; in section 3, we establish the horizontal scales and vertical structure of the dominant intraseasonal sea-level variation in the Persian Gulf; in section 4, we use dynamical theory, linear regression, and correlation analysis to identify the main local and nonlocal forcing mechanisms and ocean dynamics responsible for driving intraseasonal variations in Persian Gulf sea level and their relation to large-scale circulation and climate in the Equatorial and North Indian Ocean; we conclude with a summary and discussion in section 5.

[2]Ocean dynamic sea level is the local height of the sea surface above the geoid adjusted for the inverted-barometer effect (Gregory et al., 2019).

## 2. Materials and Methods

### a. Ocean dynamic sea level from satellite altimetry

We use version 2.0 of the sea-level essential climate variable product from the European Space Agency Climate Change Initiative (Legeais et al., 2018; Quartly et al., 2017). Data were downloaded from the Centre for Environmental Data Analysis on 18 April 2020. (All data sources are indicated in Table 1.) The multi-satellite merged geocentric sea-level anomalies are given on a 0.25° global spatial grid and a monthly time increment during 1993–2015. These data extend and update the earlier version 1.1 product (Ablain et al., 2015). The dynamic atmospheric correction is applied, which involves removing the ocean's dynamic barotropic response to wind and pressure forcing at shorter periods < 20 days and its isostatic response to pressure forcing at longer periods > 20 days from the data (Carrère and Lyard, 2003; Carrère et al. 2016). (The dynamic ocean response to these forcings at the periods of interest to this study are retained in the data.) For more details on the geophysical corrections, orbit solutions, altimeter standards, and error budgets, see Quartly et al. (2017) and Legeais et al. (2018). We remove the time series of global-mean geocentric sea-level values from every grid cell, and the resulting sea-level anomalies mainly reflect ocean dynamic sea-level anomalies. [We do not adjust the altimetry, or any other dataset, for the spatially variable effects of gravitation, rotation, and deformation related to contemporary surface ice and water mass redistribution, since these effects are negligible in this area on these timescales (Adhikari et al., 2019).] We use these data from May 2002 to September 2015, which corresponds roughly to the quasi-continuous Gravity Recovery and Climate Experiment (GRACE) record that is used for interpretation and described below. Following Gregory et al. (2019), we use $\zeta$ to denote ocean dynamic sea level.

This paper focuses on intraseasonal variability. To isolate intraseasonal behavior, we process the data as follows. We use least squares to estimate the seasonal cycle (annual and semi-annual sinusoids) and linear trend in the data over the study period. We then remove these seasonal and trend contributions from the original data to create a time series of nonseasonal residuals. Next, we apply a Gaussian smoother with a 3-month half window to these nonseasonal residuals. Finally, we subtract this low-pass-filtered time series from the nonseasonal residuals to create a record of intraseasonal fluctuations, which is the object of our study. We delete the first and last 6 months of the intraseasonal time series to avoid edge effects. This filter passes $> 90\%$ of the power at periods $\lesssim 8$ months and stops $> 70\%$ of the power at periods $\gtrsim 15$ months. See Figure 2 for an example of this filtering applied to altimetry averaged over the Persian Gulf.

*b. Manometric sea level from satellite gravimetry*

We consider data from GRACE and GRACE Follow-On (Landerer et al., 2020; Watkins et al., 2015; Wiese et al., 2016). Mass grids were downloaded from the National Aeronautics and Space Administration Jet Propulsion Laboratory on 15 April 2020 (data version JPL RL06M.MSCNv02). The data are processed using 3° spherical-cap mass-concentration blocks for the gravity-field basis functions. For more details on the estimation process, spatial constraints, scale factors, and leakage errors, see Watkins et al. (2015). The data are defined on a 0.5° global spatial grid, but the satellite measurement do not resolve processes with spatial scales $\lesssim 300$ km. We use the version of the data with the coastline resolution improvement filter applied (Wiese et al., 2016). The grids are defined at irregular, quasi-monthly increments, and have gaps. For example, battery management issues caused multi-month data gaps in the final years of GRACE, and there is a $\sim$ 1-y data gap between the end of GRACE coverage and the beginning of the GRACE Follow-On record. We linearly interpolate the available ocean mass grids onto regular monthly increments from May 2002 through September 2015. The data have units of equivalent water thickness. After correcting for global air-pressure effects, these data reflect manometric sea-level anomalies[3]. To isolate dynamic manometric sea-level anomalies associated with internal ocean mass redistribution, we subtract the time series of barystatic sea level[4] from the data at every oceanic grid cell. Intraseasonal variations are isolated through filtering methods described earlier. Following Gregory et al. (2019), we use $R_m$ to indicate manometric sea level, with its dynamic nature understood.

### *c. Relative sea level from tide gauges*

We also use monthly mean relative sea level[5] from tide-gauge records in the Persian Gulf that overlap with our study period (Table 2). Data were downloaded from the Permanent Service for Mean Sea Level database on 1 July 2019 (PSMSL, 2019; Holgate et al., 2013). The data from Mina Sulman in Manama, Bahrain represent the only record from the Persian Gulf in the PSMSL database with a complete benchmark datum history (so-called revised local reference data). To consider large-scale regional behavior, we also study a careful selection of records without continuous datum histories (so-called metric data). Namely, we use the data from Emam Hassan, Bushehr, Kangan, and Shahid Rajaee in Iran[6]. We consider the data over 2002–2006, since earlier times predate our study, and later times feature no tide-gauge data (Table 2). The data from Emam Hassan before November 2002 are omitted due to a data gap that coincided with an apparent datum shift (Alothman et al., 2014). We adjust each record for the inverted-barometer effect using

---

[3]Manometric sea-level changes indicate sea-level changes due to changes in the local mass of the ocean per unit area (Gregory et al., 2019).

[4]Barystatic sea-level changes refer to global-mean manometric sea-level changes and correspond to net addition or subtraction of water mass to or from the global ocean (Gregory et al., 2019).

[5]Relative sea level is the height of the sea surface relative to the solid Earth (Gregory et al., 2019).

[6]Metric data from other Persian Gulf locations are also available in the PSMSL database. However, we determined that these records were unsuitable for our analysis. Five records from the United Arab Emirates, Qatar, and Iraq are short and predate our study period. A dozen records from Saudi Arabia were operated by the Saudi Arabian Oil Company and situated on oil platforms, and are therefore potentially unstable.

reanalysis surface air pressure (see below). Next, we remove the seasonal cycle and linear trend from each adjusted time series. We then average together these nonseasonal time series to create a regional composite of adjusted relative sea level. Finally, we isolate intraseasonal variability by computing and then removing a low-pass-filtered version of the regional composite. The resulting time series is shown in Figure 2. To the extent that global-mean sea-level changes are unimportant, this composite time series represents tide-gauge-based intraseasonal regional $\zeta$ variability.

To establish regional context, we also consider all 53 monthly mean relative sea-level records in the PSMSL revised local reference database in the Equatorial and North Indian Ocean (40–105°E, 12.5°S–32.5°N) with $\geq$ 84 months of data during 2002–2015 ($\gtrsim$ 50% data completeness over the study period). These data are also adjusted for the inverted-barometer effect and filtered to isolate intraseasonal behavior as described above.

### *d. Surface forcing*

We use gridded observations, atmospheric reanalyses, and flux estimates to interpret the data from altimetry, GRACE, and tide gauges. For all fields, we compute intraseasonal anomalies during 2002–2015 from the available monthly values, as with the altimetry and GRACE.

We use monthly wind stress and barometric pressure from the European Centre for Medium Range Weather Forecasts Reanalysis Interim (ERA-Interim; Dee et al., 2011). Fields were downloaded from the Woods Hole Oceanographic Institution (WHOI) Community Storage Server on 7 January 2019. Values are defined on a 0.75° global spatial grid from January 1979 to October 2018.

We use monthly evaporation from version 3 of the the Objectively Analyzed air-sea Fluxes project (OAFlux; Yu and Weller, 2007). Fields were downloaded from WHOI servers on 13 November 2019. Values are defined on a 1° global spatial grid from January 1958 to December 2018.

We use monthly precipitation from version 2.3 of the Global Precipitation Climatology Project (GPCP; Adler et al., 2003). Fields were downloaded from National Oceanic and Atmospheric Administration Earth System Research Laboratory and Physical Sciences Laboratory on 16 April 2020. Values are defined on a 2.5° global spatial grid from January 1979 to the present.

We use monthly river runoff from the Japanese 55-year atmospheric reanalysis surface data set for driving ocean–sea-ice models (JRA55-do; Tsujino et al., 2018). Fields were downloaded from servers at the Hokkaido University Graduate School of Environmental Science on 21 August 2020. Values are defined on a 0.25° global coastal grid from January 1958 to December 2017.

## 3. Horizontal scales and vertical structure of $\zeta$ variability

Past studies use satellite altimetry and tide gauges to study seasonal cycles and decadal trends in the Persian Gulf (Al-Subhi, 2010; Alothman et al., 2014; Ayhan, 2020; El-Gindy, 1991; El-Gindy and Eid, 1997; Hassanzadeh et al., 2007; Hosseinibalam et al., 2007; Sharaf El Din, 1990; Siddig et al., 2019; Sultan et al., 1995a, 2000). Here we examine intraseasonal variability in the Persian Gulf using satellite data, including altimetry but also gravimetry, and tide gauges.

We motivated this study with an exploratory data analysis earlier in the Introduction. We found that roughly half of the monthly $\zeta$ variance from altimetry averaged over the Persian Gulf during 2002–2015 was concentrated at intraseasonal periods, and that the Persian-Gulf-average altimetric time series of intraseasonal $\zeta$ ($\overline{\zeta}$) explained about half of the variance in a composite time series of intraseasonal $\zeta$ from coastal tide gauges (Figure 2). These results show that intraseasonal fluctuations contribute importantly to large-scale $\zeta$ variability over the Persian Gulf at monthly to decadal periods, and that intraseasonal fluctuations measured locally at the coast largely reflect spatially coherent, basin-wide behavior.

To explore intraseasonal $\zeta$ in more detail, we apply empirical orthogonal function (EOF) analysis to altimetry data over the Persian Gulf. We identify the spatial structures and temporal behaviors of the orthogonal modes of intraseasonal variability by solving for the eigenvalues and eigenvectors of the covariance matrix of the altimetry data over the Persian Gulf. The eigenvectors correspond to the spatial structures and the eigenvalues indicate the amounts of data variance explained by the various modes. The temporal behaviors of the modes are described by principal-component time series, which are determined by projecting the respective eigenvectors onto the data (von Storch and Zwiers, 1999).

The leading mode, which explains 52% of the intraseasonal data variance over the Persian Gulf, is summarized in Figures 3 and 4. It shows a single-signed spatial structure (Figure 3a), indicating basin-wide variation and wholesale raising and lowering of $\zeta$ over the Persian Gulf. This is consistent with our earlier finding that the $\overline{\zeta}$ time series from altimetry explains 51% of the variance in the regional composite from tide gauges at intraseasonal timescales (Figure 2). Indeed, this mode's principal-component time series (Figure 4) is perfectly correlated with the $\overline{\zeta}$ time series from altimetry (correlation coefficient > 0.99). The leading mode from a complex-valued (Hilbert) EOF analysis explains the same amount of data variance (not shown). This means that out-of-phase relationships between $\zeta$ in different parts of the Persian Gulf related to signal propagation are unimportant to this mode, and that this dominant $\zeta$ variation reflects an in-phase standing mode of oscillation across the region on these timescales.

The spatial structure is also nonuniform (Figure 3a). Magnitudes increase from southeast to northwest across the region, with smaller values (1–3 cm) observed along the United Arab Emirates, Qatar, Bahrain, and southern Iran, and larger values (3–5 cm) apparent off Saudi Arabia, Kuwait, Iraq, and northern Iran. This basin-scale structure could indicate a balance between local wind forcing—strengthening or weakening of the region's prevailing north-northwesterlies—and the combined effects of bottom friction and along-basin pressure gradient. Strongest amplitudes (> 5 cm) are detected off Kuwait and Iraq. Values in this region are highest at the coast and decay offshore. Since depths become shallow and bathymetric gradients weak off Kuwait and Iraq relative to upstream along Iran (Figure 1), these strong amplitudes may indicate coastal-wave amplification related to shoaling and broadening of the topography in this region (e.g., Hughes et al., 2019). It is also possible, as the region is adjacent to the mouths of the Tigris, Euphrates, and Karun rivers, that trapped $\zeta$ signals driven by buoyant river discharge also come into play (e.g., Piecuch et al., 2018a). There is also spatial structure in the amount of local data variance explained by this mode: whereas 50–80% of local $\zeta$ data variance is explained over the interior in the northwestern Persian Gulf, < 30% is explained in the southwest off Qatar, Bahrain, and the United Arab Emirates (Figure 3b). This suggests important local-scale $\zeta$ variability along the southwest coast that is unrelated to the broader-scale behavior resolved by this mode.[7]

The $\zeta$ response to surface forcing is often described in terms of barotropic (depth-independent) and baroclinic (depth-dependent) adjustments (e.g., Vinogradova et al., 2007). Given the latitude of the Persian Gulf, and the spatiotemporal scales under investigation, basic scaling arguments (Gill and Niiler, 1973; Piecuch et al., 2019) suggest that this mode of $\zeta$ variation should be essentially barotropic in nature. For a purely barotropic ocean response, changes in sea level (or subsurface pressure) are mirrored by changes in ocean bottom pressure (Bingham and Hughes, 2008; Vinogradova et al., 2007). Hence, if the leading mode of $\zeta$ variability from altimetry

[7]Indeed, the second EOF mode (not shown), which explains 8% of the data variance, captures some of the variability in these areas. This mode exhibits amplitudes > 5 cm and explains > 30% of the data variance off western Qatar, around Bahrain, and along southeastern Saudi Arabia, whereas amplitudes of 2–3 cm and variances explained of 5–30% are apparent in the Southern Shallows off the United Arab Emirates. Since it is tangential to our focus, we do not pay further attention to this mode, other than to posit that—due to the region's broad, shallow depths (Figure 1)—it may arise from a balance between local winds and bottom friction.

(Figure 3, 4) reflects a predominantly barotropic response, then similar $R_m$ variability should be apparent in GRACE.

To test this hypothesis, we apply EOF analysis to the GRACE $R_m$ grids over the Persian Gulf. The results are shown in Figures 4 and 5. The leading mode, which explains 88% of the intraseasonal GRACE data variance in the Persian Gulf, shows a single-signed spatial pattern, such that variability increases from 1–2 cm in the southeastern Persian Gulf to 3–4 cm in the northwest (Figure 5a). Relatively more local $R_m$ data variance is explained (> 80%) to the north and west, while comparatively less is explained (50–70%) in the southeast (Figure 5b). These patterns from GRACE are qualitatively similar to those from altimetry, but there are quantitative differences (cf. Figures 3, 5). For example, the mode from altimetry exhibits larger amplitudes and richer, more detailed spatial structures than the mode from GRACE (Figures 3a, 5a), whereas the leading GRACE mode explains relatively more data variance compared to the leading altimetry mode (Figures 3b, 5b). These discrepancies probably partly reflect the coarser resolution (and reduced effective spatial degrees of freedom) of GRACE, but could also indicate baroclinic processes or data errors (e.g., residual leakage of terrestrial signals into the GRACE ocean grids).

Such differences notwithstanding, results in Figures 3 and 5 suggest that GRACE and altimetry capture facets of the same underlying mode of intraseasonal variation. This suggestion is corroborated by the principal components of the leading EOF modes determined from GRACE and altimetry, which are highly correlated (correlation coefficient of $\sim 0.7$; Figure 4). We also apply maximum covariance analysis (MCA) jointly to altimetry $\zeta$ and GRACE $R_m$ data, whereby the eigenvalues and eigenvectors of the cross-covariance matrix between the two data sets are determined (von Storch and Zwiers, 1999). The leading eigenvectors and principal components determined jointly through MCA are identical to those determined separately through EOF analysis, and the gravest MCA mode explains > 99% of the joint covariance between altimetry and

GRACE data (not shown). This suggests that the leading modes of regional $\zeta$ and $R_m$ variation are coupled to one another, and reflect a dominant barotropic response.

## 4. Forcing mechanisms and ocean dynamics

In the previous section, we established a basin-wide barotropic variation of the Persian Gulf on intraseasonal timescales. Here we use analytical theory, linear regression, and correlation analysis to identify the forcing and dynamics responsible for this mode.

### *a. Linear barotropic model*

The leading mode of intraseasonal variability identified previously exhibits higher-order spatial structure (Figures 3, 5). However, the lowest-order spatial feature is that of a horizontally uniform fluctuation. For example, the time series of intraseasonal $\overline{\zeta}$ from altimetry explains 93% of the variance associated with the first altimetric EOF mode (Figures 2–4). Thus, we formulate a linear model for a horizontally uniform barotropic variation of the Persian Gulf. Our formulation largely follows Volkov et al. (2016), who use a similar model to consider $\zeta$ in the Black Sea. The equations for conservation of volume within the Persian Gulf and conservation of momentum along the Strait of Hormuz are

$$S\overline{\zeta}_t = S\overline{q} + \frac{S}{\rho g}\overline{p}_t + vWH, \tag{1}$$

$$v_t = -g\zeta_y + \frac{1}{\rho H}\tau - \frac{r}{H}v. \tag{2}$$

Here $S$ is surface area of the Persian Gulf, overbar is spatial average over the Persian Gulf, $q$ is precipitation plus runoff minus evaporation, $p$ is barometric pressure, $v$ is average velocity along the Strait of Hormuz into the Persian Gulf (positive values increase the volume of the Persian Gulf), $W$ and $H$ are the width and depth of the Strait of Hormuz, respectively, $\tau$ is wind stress along the Strait of Hormuz (positive in the direction of the Persian Gulf), $r$ is a constant friction coefficient,

$g$ is gravity, $\rho$ is seawater density, and subscripts $t$ and $y$ denote partial differentiation in time and the along-strait direction, respectively. Note that, since we express Eqs. (1) and (2) in terms of $\zeta$, forcing by $p$ appears in the continuity equation rather than in the momentum equation, and takes on a form analogous to the $q$ forcing, such that, as noted by Gill (1982), forcing by a depression of 10 mb would be canceled out by 10 cm of precipitation (cf. also Ponte, 2006). All symbols are described in Table 3 and representative values are given when appropriate.

We assume $\zeta$, $v$, $q$, $p$, and $\tau$ take wave solutions of the form $\exp(-i\omega t)$ with angular frequency $\omega$ and $i \doteq \sqrt{-1}$. Integrating the momentum equation over the length $L$ of the Strait of Hormuz, and rearranging to solve for $\overline{\zeta}$ gives

$$\overline{\zeta} = \left[\zeta_0 + \frac{L}{\rho g H}\tau + \frac{(\lambda - i\omega)}{\sigma^2}\overline{q} - i\omega\frac{(\lambda - i\omega)}{\sigma^2}\frac{\overline{p}}{\rho g}\right] \Bigg/ \left[1 - \frac{\omega^2}{\sigma^2} - i\frac{\lambda\omega}{\sigma^2}\right], \tag{3}$$

where $\zeta_0$ represents $\zeta$ at the boundary outside the Strait of Hormuz in the Gulf of Oman, and we define $\sigma^2 \doteq WHg/SL$ and $\lambda \doteq r/H$. Physically, $1/\lambda$ is a friction timescale and $1/\sigma$ is a Helmholtz resonance timescale determined by the shape of the Persian Gulf and Strait of Hormuz. (We determine that $1/\sigma \approx 15$ hours, which is small compared to the intraseasonal timescales of interest, so we do not expect a resonant response.) Equivalently, we can write Eq. (3) in the polar complex plane as

$$\overline{\zeta} = z_{\zeta_0}\exp\left(i\theta_{\zeta_0}\right)\zeta_0 + z_\tau \exp(i\theta_\tau)\tau + z_{\overline{q}}\exp\left(i\theta_{\overline{q}}\right)\overline{q} + z_{\overline{p}}\exp\left(i\theta_{\overline{p}}\right)\overline{p}, \tag{4}$$

where

$$\theta_{\zeta_0} \doteq \arctan\left(\frac{\lambda\omega}{\sigma^2 - \omega^2}\right), \tag{5}$$

$$z_{\zeta_0} \doteq \left[\left(1 - \frac{\omega^2}{\sigma^2}\right)^2 + \left(\frac{\lambda\omega}{\sigma^2}\right)^2\right]^{-1/2}, \tag{6}$$

$$\theta_\tau \doteq \arctan\left(\frac{\lambda\omega}{\sigma^2 - \omega^2}\right), \tag{7}$$

$$z_{\tau} \doteq \left[ \left(1 - \frac{\omega^2}{\sigma^2}\right)^2 + \left(\frac{\lambda\omega}{\sigma^2}\right)^2 \right]^{-1/2} \left(\frac{L}{\rho g H}\right), \tag{8}$$

$$\theta_{\overline{q}} \doteq \arctan\left(\frac{\lambda\omega}{\sigma^2} - \frac{\omega}{\lambda} + \frac{\omega^3}{\sigma^2\lambda}\right), \tag{9}$$

$$z_{\overline{q}} \doteq \frac{\lambda}{\sigma^2} \left[ 1 + \left(\frac{\lambda\omega}{\sigma^2} - \frac{\omega}{\lambda} + \frac{\omega^3}{\sigma^2\lambda}\right)^2 \right]^{1/2} \left[ \left(1 - \frac{\omega^2}{\sigma^2}\right)^2 + \left(\frac{\lambda\omega}{\sigma^2}\right)^2 \right]^{-1}, \tag{10}$$

$$\theta_{\overline{p}} \doteq \arctan\left[ \left(\frac{\omega}{\lambda} - \frac{\omega^3}{\lambda\sigma^2} - \frac{\omega\lambda}{\sigma^2}\right)^{-1} \right], \tag{11}$$

$$z_{\overline{p}} \doteq \frac{1}{\rho g} \frac{\lambda\omega}{\sigma^2} \left[ 1 + \left(\frac{\omega}{\lambda} - \frac{\lambda\omega}{\sigma^2} - \frac{\omega^3}{\sigma^2\lambda}\right)^2 \right]^{1/2} \left[ \left(1 - \frac{\omega^2}{\sigma^2}\right)^2 + \left(\frac{\omega\lambda}{\sigma^2}\right)^2 \right]^{-1}, \tag{12}$$

In other words, according to Eq. (4), $\overline{\zeta}$ is a linear superposition of the $\zeta_0$, $\tau$, $\overline{q}$, and $\overline{p}$ forcing terms, each scaled by an amount $z_j$ and rotated through a phase $\theta_j$, where $j \in \{\zeta_0, \tau, \overline{q}, \overline{p}\}$. We estimate theoretical values for the scaling factors $z_j$ and phase angles $\theta_j$ by averaging Eqs. (5)–(12) over the $\omega$ range from $2\pi/$(6 months) to $2\pi/$(2 months) using numerical values for the scalar coefficients $\lambda$, $\sigma$, $L$, $\rho$, $g$, and $H$ from Table 3. These theoretical values are tabulated in Table 4.

### *b. Multiple linear regression analysis*

To test whether the model described by Eqs. (1)–(12) is informative for understanding observed intraseasonal $\overline{\zeta}$ variability, we perform a multiple linear regression. We model $\overline{\zeta}$ from altimetry as

$$\overline{\zeta} = a_{\zeta_0}\zeta_0 + b_{\zeta_0}\mathcal{H}(\zeta_0) + a_{\tau}\tau + b_{\tau}\mathcal{H}(\tau) + a_{\overline{q}}\overline{q} + b_{\overline{q}}\mathcal{H}(\overline{q}) + a_{\overline{p}}\overline{p} + b_{\overline{p}}\mathcal{H}(\overline{p}) + \varepsilon, \tag{13}$$

where $\mathcal{H}$ is the Hilbert transform, the $a_j$ and $b_j$ are real constants, and $\varepsilon$ is the residual. We include Hilbert transforms of the various forcings in the regression to allow for possible phase lags between the forcing and the response, as indicated by Eq. (4). We estimate the $z_j$ and $\theta_j$ from Eq. (4) from the $a_j$ and $b_j$ in Eq. (13) using properties of Hilbert transforms and trigonometric identities as

$$\theta_j = \arctan\left(b_j / a_j\right), \tag{14}$$

$$z_j = \sqrt{a_j^2 + b_j^2}. \tag{15}$$

We evaluate Eq. (13) using least squares. For $\zeta_0$, we use $\zeta$ from altimetry averaged over shallow regions (< 200 m) of the northern Gulf of Oman outside the Strait of Hormuz (57–60°E, 25–28°N). For $\tau$, we use along-strait wind stress (315°T) from ERA-Interim averaged over the Strait of Hormuz (54–57.8°E, 22.9–27.4°N). For $\overline{q}$, we use precipitation from GPCP plus river runoff from JRA55-do minus evaporation from OAFlux averaged over the Persian Gulf (45–55°E, 24–32°N). For $\overline{p}$, we use barometric pressure from ERA-Interim averaged over the Persian Gulf (48–54.8°E, 24.4–29.6°N). Uncertainties are estimated using 10 000 iterations of bootstrapping (Efron and Hastie, 2016).

Results of the multiple linear regression are summarized in Figure 6. The regression model [(13)] explains 70% ± 9% (95% confidence interval) of the variance in the $\overline{\zeta}$ data (Figure 6a). This suggests that Eqs. (1) and (2) represent the dominant physics, and that $\overline{\zeta}$ variability can be largely understood in terms of local surface forcing by $\tau$, $\overline{q}$, and $\overline{p}$ and nonlocal boundary forcing by $\zeta_0$. In Figure 6b, we break down the relative contributions of the different forcing terms. The primary driver of $\overline{\zeta}$ is nonlocal forcing by $\zeta_0$, which explains 50% ± 12% of the $\overline{\zeta}$ variance. Local forcing by $\tau$, $\overline{q}$, and $\overline{p}$ plays a secondary role. Individually, $\tau$ explains 16% ± 9%, $\overline{q}$ explains 5% ± 9%, and $\overline{p}$ explains 10% ± 8% of the $\overline{\zeta}$ variance. Surface loading (the combination of $\overline{q}$ and $\overline{p}$ forcing) explains 14% ± 11% of the variance in the data. Collectively, all three local forcing factors taken together account for 27% ± 14% of the $\overline{\zeta}$ variance.[8]

[8]The variance contributions of the individual predictors are not entirely additive, since they are not wholly independent and there is some correlation between them. However, the relative roles of the respective forcings can nevertheless be meaningfully estimated (albeit with uncertainty) because the least-squares problem is generally well posed. After normalizing the predictors to unit variance, the condition number of their covariance matrix is 3.3. This is on the same order as the range of 1.4–2.5 (99% confidence interval) we determine through repeated simulations of four independent random, standard-normal time series (and their Hilbert transforms) with the same length as the observations (not shown).

Regression coefficients computed empirically from the data are consistent with values expected theoretically from first principles (Table 4). For example, the linear regression yields a scaling factor of $1.5 \pm 0.5$ m Pa$^{-1}$ and a phase angle of $30 \pm 25$ degrees between $\tau$ and $\overline{\zeta}$. This is consistent with the theoretical ranges of 1.0–1.3 m Pa$^{-1}$ and 5–38 degrees anticipated from Eqs. (7) and (8). The regression analysis also suggests a substantial departure from the inverted-barometer response, manifested in a scaling of $0.8 \pm 0.5$ cm mb$^{-1}$ and a phase of $65 \pm 52$ degrees between $\overline{p}$ and $\overline{\zeta}$. This overlaps with the ranges of 0.1–0.5 cm mb$^{-1}$ and 56–87 degrees expected from Eqs. (11) and (12). (Recall that the altimeter data have been adjusted for an inverted barometer and that our theory was developed for $\zeta$, which has the inverted-barometer effect already removed.) This provides evidence that the results of the multiple linear regression indicate true causal relationships between forcing and response.

Regression results and analytical theory suggest that these relationships can be out of phase, such that the forcings lead the response by a significant amount (Table 4). To quantify the importance of out-of-phase behavior, we perform another multiple linear regression analysis, this time omitting Hilbert transforms and forcing by $p$ from the input [cf. Eq. (13)]. Physically, this alternative regression model assumes an equilibrium response, and corresponds to the steady state ($\omega \to 0$) limit of the governing equations, viz. [cf. Eq. (3)],

$$\overline{\zeta} = \zeta_0 + \frac{L}{\rho g h}\tau + \frac{\lambda}{\sigma^2}\overline{q}. \tag{16}$$

This alternate model accounts for slightly less of the $\overline{\zeta}$ data variance (62% ± 10%; 95% confidence interval). This result demonstrates that a majority of the $\overline{\zeta}$ data variance explained by the original multiple linear regression model [Eq. (13)] is attributable to equilibrium processes and in-phase (or antiphase) relationships between the forcing and the response, but also that allowing for transient processes [the time derivatives in Eqs. (1) and (2)] and more general phase relationships between forcing and response leads to a modest, but significant, improvement in terms of explaining $\overline{\zeta}$ data variance.

To ascertain whether similar balances are expected at other periods, we consider the $\overline{\zeta}$ response from our model as a function of timescale. We multiply the frequency-dependent scale coefficients [$z_j$ in Eqs. (6), (8), (10), (12)] by a representative fluctuation in the respective forcing [cf. Eq. (4)]. We use $|\zeta_0| = 2$ cm, $|\tau| = 0.005$ N m$^{-2}$, $|\overline{q}| = 1 \times 10^{-8}$ m s$^{-1}$, and $|\overline{p}| = 0.5$ hPa based on standard deviations computed from the data. Results are shown in Figure 7. As demanded by Eqs. (6), (8), (10), (12), the $\overline{\zeta}$ responses to $\zeta_0$, $\tau$, and $\overline{q}$ forcing increase with period, while the $\overline{\zeta}$ adjustment to $\overline{p}$ driving generally decreases with period. The precise rate at which the $\overline{\zeta}$ adjustment approaches its equilibrium response is dictated by friction and the region's shape, as represented by $\lambda$ and $\sigma$. Given the forcing amplitudes, $\overline{\zeta}$ variability is dominated by $\overline{p}$ forcing on timescales of a few days. On timescales of a few days to a few weeks, the influences of $\overline{p}$, $\tau$, and $\zeta_0$ on $\overline{\zeta}$ can be comparable, depending on the details of friction. At periods longer than a few weeks, forcing by $\zeta_0$ is the primary driver of $\overline{\zeta}$ variability. At all periods, $\zeta_0$ forcing is more influential than $\tau$ and $\overline{q}$ forcing. Thus, our findings on intraseasonal timescales are representative of the large-scale, low-frequency barotropic response of the Persian Gulf to external forcing more broadly. This suggests that similar dynamical balances would be obtained in studies of the Persian Gulf over longer timescales. But note that our results are a function of the forcing amplitudes, geometry of the region, and friction. For example, assuming similar friction values and forcing scales, $\tau$ and $\overline{q}$ forcing would become relatively more important compared to $\zeta_0$ forcing for a marginal sea with a larger surface area than the Persian Gulf that connects to the open ocean through a strait that is longer, shallower, and narrower than the Strait of Hormuz.

*c. Relation to Indian Ocean circulation and climate, and potential predictability*

Nonlocal forcing by $\zeta_0$ is the most important contributor to $\overline{\zeta}$ variability (Figures 6b, 7). What is the nature of these fluctuations at the boundary in the Gulf of Oman? How do they relate to larger-scale circulation and climate? To clarify their origin, we compute correlation coefficients between $\zeta_0$ and either $\zeta$ or its Hilbert transform $\mathcal{H}(\zeta)$ at every altimetric grid point over the Equatorial and North Indian Ocean. Correlations between $\zeta_0$ and $\zeta$ identify regions where $\zeta$ is in phase or anti-phase (i.e., 180 degrees out of phase) with $\zeta_0$, whereas correlations between $\zeta_0$ and $\mathcal{H}(\zeta)$ indicate regions where $\zeta$ is in quadrature (90 degrees out of phase) or anti-quadrature (270 degrees out of phase) with $\zeta_0$.

In general, $\zeta_0$ is uncorrelated with $\zeta$ and $\mathcal{H}(\zeta)$ away from the coast and the equator (Figures 8, 9), suggesting that $\zeta_0$ is unrelated to the dominant $\zeta$ variability in these open-ocean regions. However, we observe patterns of significant correlation and anti-correlation along the coast and equator. For example, $\zeta_0$ is correlated with $\zeta$ along Pakistan, western India, and Sri Lanka; correlated with $\mathcal{H}(\zeta)$ along eastern India, Bangladesh, and Myanmar; correlated with $\mathcal{H}(\zeta)$ and anti-correlated with $\zeta$ along Thailand, Malaysia, and Sumatra; and anti-correlated with $\mathcal{H}(\zeta)$ along the western equatorial Indian Ocean between Somalia and the Maldives (Figures 8, 9). Similar correlation patterns are observed between $\zeta_0$ and available tide-gauge data over the Equatorial and North Indian Ocean (Figure 8). Given the gaps in the data, we do not compute Hilbert transforms from the tide-gauge records. [Note also that we computed correlations with altimetry more globally over the ocean, but did not observe large-scale regions of significant correlation between $\zeta_0$ and $\zeta$ or $\mathcal{H}(\zeta)$ outside of the Equatorial and North Indian Ocean that suggested viable causal connections (not shown).]

These patterns suggest wave propagation along equatorial and coastal waveguides. For example, the correlation between $\zeta_0$ and $\mathcal{H}(\zeta)$ along Bangladesh suggests that $\zeta_0$ lags $\zeta$ in this region by 90 degrees (one quarter of a period), whereas anti-correlation between $\zeta_0$ and $\mathcal{H}(\zeta)$ in the western equatorial Indian Ocean hints that regional $\zeta$ leads $\zeta_0$ by 270 degrees (three quarters of a period). Supposing propagation is eastward along the equator and counterclockwise along the coast (in the Northern Hemisphere), and assuming intraseasonal periods of 60–180 days, we estimate that these phase leads and lags imply propagation speeds of $\sim$ 1–3 m s$^{-1}$. These values are consistent with basic expectations for equatorial waves and coastally trapped waves (e.g., Gill, 1982; Hughes et al., 2019). Indeed, past studies argue that low-latitude wind forcing associated with the Madden-Julian oscillation (MJO) and phases of the monsoon excite wave responses that effect intraseasonal sea-level variability along Sumatra and Java (Iskandar et al., 2005), the Bay of Bengal (Cheng et al., 2013), and India and Sri Lanka (Suresh et al., 2013; Dhage and Strub, 2016). Our results reinforce these past findings, and suggest that these nonlocal forcing effects mediated by large-scale wave responses continue on and are communicated to the Persian Gulf.

We perform a similar analysis with GRACE data. Correlations between $\zeta_0$ and either GRACE $R_m$ or its Hilbert transform $\mathcal{H}(R_m)$ over the Indian Ocean are shown in Figure 10. While there is essentially no meaningful correlation anywhere between $\zeta_0$ and $\mathcal{H}(R_m)$, there is significant correlation between $\zeta_0$ and GRACE $R_m$ broadly over much of the Indian Ocean (Figure 10). This suggests that $\zeta_0$ is also related to a basin-scale equilibrium response in addition to the more transient wave adjustments trapped to the coast and the equator suggested by the altimetry data (Figures 8, 9). Indeed, the correlation pattern between $\zeta_0$ and $R_m$ (Figure 10a) is similar to the spatial structure of the intraseasonal fluctuation of the Indian Ocean identified by Rohith et al. (2019) based on data from bottom-pressure recorders, GRACE, and a general circulation model. They argue that wind-curl fluctuations at 30–80-day periods over the Wharton basin associated with the MJO excite planetary and topographic Rossby wave responses that lead to a basin-wide barotropic variation that is confined to the Indian Ocean by bathymetric contours. Our results provide observational evidence that this large-scale intraseasonal fluctuation affects variability not only over the deep Indian Ocean but also within its shallow marginal seas.

Wave propagation apparent in Figures 8 and 9 hints that $\zeta_0$ variability may be predictable to some extent. That is, armed with upstream $\zeta$ information, it may be possible to anticipate $\zeta_0$ variance in advance. To test this possibility, we compute lagged correlation coefficients between $\zeta_0$ and $\zeta$ at earlier times over the Equatorial and North Indian Ocean. Results are shown in Figures 11 and 12 for lead times of 1 and 2 months, respectively. Considering a 1-month lead time, we find positive correlations between $\zeta_0$ and $\zeta$ upstream along the Indian Subcontinent and Maritime Continent, from eastern India to Sumatra, and negative correlations over the western Equatorial Indian Ocean between Somalia and the Maldives (Figure 11). Indeed, the pattern of correlation between $\zeta_0$ and $\zeta$ 1 month earlier is similar to the structure of correlation between $\zeta_0$ and $\mathcal{H}(\zeta)$ (cf. Figures 9, 11), suggesting a dominant timescale of $\sim 4$ months. Values of 0.4–0.5 are apparent off Myanmar and Sumatra (Figure 11), hinting that 16–25% of the variance in $\zeta_0$ can be predicted from $\zeta$ knowledge in these regions 1 month earlier. Considering a lead time of 2 months, we observe that $\zeta_0$ and $\zeta$ are largely uncorrelated, except for along Pakistan, western India, and Sri Lanka, where negative coefficients between $-0.3$ and $-0.4$ are seen. This implies that 9–16% of the $\zeta_0$ variance can be predicted from $\zeta$ observations along this coastline 2 months earlier. Considering lead times of 3 months and longer, we detect no significant correlations between $\zeta_0$ and $\zeta$ elsewhere (not shown), indicating that there is little skill in predictions of intraseasonal $\zeta_0$ variability more than 2 months into the future from wave characteristics and ocean memory alone. Considering the available tide-gauge records in the Equatorial and North Indian Ocean, we obtain similar patterns of lagged correlations (Figures 11, 12).

## 5. Summary and discussion

We studied intraseasonal variability in ocean dynamic sea level ($\zeta$) over the Persian Gulf during 2002–2015 using satellite observations and other data (Figures 1, 2). Intraseasonal $\zeta$ variability in the Persian Gulf manifests in a basin-wide, vertically coherent mode of fluctuation (Figures 3–5). This large-scale mode is related to freshwater flux and barometric pressure over the Persian Gulf, wind stress along the Strait of Hormuz, and nonlocal forcing embodied in $\zeta$ variations at the boundary in the Gulf of Oman (Figures 6, 7). The $\zeta$ boundary condition shows rich correlation patterns with altimetry data upstream along the Indian Subcontinent, Maritime Continent, and equatorial Indian Ocean (Figures 8, 9), and with GRACE data broadly over the Indian Ocean (Figure 10), suggesting an intimate connection between intraseasonal $\zeta$ variability in the Persian Gulf and large-scale circulation and climate in the Equatorial and North Indian Ocean mediated by equatorial-, Rossby-, and coastal-wave processes identified previously (Cheng et al., 2013; Dhage and Strub, 2016; Iskandar et al., 2005; Oliver and Thompson, 2010; Rohith et al., 2019; Suresh et al., 2013, 2016; Waliser et al., 2003, 2004). Our results indicate that some intraseasonal $\zeta$ variance in the Persian Gulf may be predictable a month or so in advance from upstream observations and the physics of coastal wave propagation and ocean memory (Figures 11, 12).

Our results establish the dominant magnitudes, scales, and mechanisms of intraseasonal sea-level variability in the Persian Gulf, and thus build on findings from past works that emphasize seasonal cycles and decadal trends (Al-Subhi, 2010; Alothman et al., 2014; Ayhan, 2020; El-Gindy, 1991; El-Gindy and Eid, 1997; Hassanzadeh et al., 2007; Hosseinibalam et al., 2007; Sharaf El Din, 1990; Siddig et al., 2019; Sultan et al., 1995a, 2000). Our study demonstrates that GRACE satellite retrievals are informative for interrogating coastal sea level over a semi-enclosed marginal sea, thereby complementing previous efforts that demonstrate the value of GRACE data in other marginal seas (Feng et al., 2012, 2014; Fenoglio-Marc et al., 2006, 2012; Landerer and Volkov, 2013; Loomis and Luthcke, 2017; Piecuch and Ponte, 2015; Piecuch et al., 2018b; Tregoning et al., 2008; Wahr et al., 2014; Wang et al., 2015; Wouters and Chambers, 2010), and encouraging further exploration of GRACE data in the Persian Gulf at other timescales.

Intraseasonal $\zeta$ variability in the Persian Gulf is coupled to variable volume exchanges between the Persian Gulf and Arabian Sea through the Strait of Hormuz. Observations of the time-variable transport through the Strait of Hormuz are limited to short field campaigns (e.g., Johns et al., 2003). Therefore, it is informative to consider the transport variability implied by data here and permitted by our model. Based on volume conservation [Eq. (1)], we make a rough estimate of the variable transport using our time series of surface freshwater flux and time derivatives of $\zeta$ and air pressure (not shown). The standard deviation of the transport estimate is $2.7 \times 10^3$ m$^3$ s$^{-1}$. In relative terms, this represents a departure of 19–28% from the steady state transport required to balance canonical values for the average evaporation over the Persian Gulf of 1.4–2 m y$^{-1}$ (Privett, 1959; Ahmad and Sultan, 1990; Johns et al., 2003). These transport fluctuations arise from subtle velocity variations averaged over the width and depth of the Strait of Hormuz of only $\sim 0.9$ mm s$^{-1}$. An interrogation of our model equations [Eqs. (1) and (2)] suggests that these variations in transport result mainly from a combination of local surface freshwater flux and nonlocal forcing at the boundary over the Gulf of Oman (see Appendix).

This investigation advances knowledge of sea-level variability in the Persian Gulf. It also paves the way for future studies, pointing to open questions. For example, we developed and tested a theory for a horizontally uniform fluctuation of the Persian Gulf. However, the leading mode of intraseasonal $\zeta$ variability in the region exhibits spatial structure, such that magnitudes are larger in the northwest and smaller in the southeast of the Persian Gulf (Figures 3, 5). We hypothesized that this spatial structure could arise from local surface forcing or topographic effects on coastal-wave propagation. Future studies based on high-resolution ocean models should test these hypotheses and identify the controls on spatial structure.

It also remains to quantify whether baroclinic effects and steric processes contribute to the dominant intraseasonal $\zeta$ variability in the Persian Gulf. Vertical density stratification in the region is stronger during summer than during winter (Reynolds, 1993), and offshore bathymetric gradients are more dramatic to the east along Iran than to the north, west, and south along other Persian-Gulf nations (Figure 1). Coastal wave theory (Hughes et al., 2019, and references therein) suggests that such conditions favor barotropic (topographic) wave $\zeta$ adjustment in wintertime or along the coast from Iraq to Oman, but that baroclinic (Kelvin) wave $\zeta$ response may be relevant along the coast of Iran in summertime. Local surface heat fluxes could also effect important variations in density and steric height. For example, fluctuations in evaporation of $\pm 1 \times 10^{-8}$ m s$^{-1}$ (cf. Figures 6, 7) correspond to variations in latent heat flux of ±25 W m$^{-2}$ [see Eq. (4a) in Large and Yeager, 2004], which, if sustained for periods of 60–180 d, would result in fluctuations in steric height of 2–5 mm [see Eq. (8) in Vivier et al., 1999]. Steric changes were not estimated due to the lack of continuous hydrographic records in the Persian Gulf (e.g., Good et al., 2013). However, future studies could explore this topic by comparing differences between altimetry and GRACE, which are potentially informative of steric processes, to sea-level changes anticipated from the passive response to local surface heat flux (e.g., Cabanes et al., 2006), or sea-surface temperature data assuming that ocean temperature variations are vertically coherent (e.g., Meyssignac et al., 2017).

We determined that dynamic response to barometric pressure and freshwater flux is a secondary but nevertheless significant contributor to intraseasonal $\zeta$ variability in the Persian Gulf (Figure 6). This is interesting, given that the barotropic ocean response to surface loading is generally expected to be isostatic on timescales longer than a few days (e.g., Wunsch and Stammer, 1997; Ponte, 2006). In our model physics, the dynamic response is permitted by friction through the Strait of Hormuz.

Our finding that freshwater flux elicits a $\zeta$ response on the order of a few mm (Figure 6) is consistent with the basic $\zeta$ magnitudes simulated for this region across subdaily to annual timescales by Ponte (2006) using a 1-year simulation from a global barotropic ocean general circulation model forced with evaporation and precipitation (Hirose et al., 2001); however, that model was designed for global studies, and it used coarse resolution ($\sim 1^\circ$) and a large friction coefficient ($2 \times 10^{-2}$ m s$^{-1}$), which may not accurately capture important physics in and around the Persian Gulf. Future studies using high-resolution ocean models would be informative for clarifying the nature of intraseasonal $\zeta$ variation in the Persian Gulf and the role of surface loading. Also relevant here is the fact that the non-isostatic response to barometric pressure is roughly in quadrature with the forcing (Table 4). This highlights the importance of considering phase information when testing for departures from a pure inverted-barometer response in sea-level data (e.g., Mathers and Woodworth, 2001, 2004).

Past studies argue that low-latitude wind forcing of the Indian Ocean related to large-scale climate modes excites wave responses that effect intraseasonal sea-level variability along the Indian Subcontinent and Maritime Continent, from Sumatra to western India (Cheng et al., 2013; Dhage and Strub, 2016; Iskandar et al., 2005; Suresh et al., 2013). We provide evidence that these coastal-trapped waves continue propagating downstream and influence sea level in the Gulf of Oman and Persian Gulf (Figures 8, 9). We acknowledge that, while they suggest wave propagation, Figures 8 and 9 could alternatively indicate the spatial scales of the atmospheric forcing. For example, large-scale wind forcing along the equator and off the southern tip of the Indian subcontinent could simultaneously excite equatorial waves and coastal waves propagating in the cyclonic sense along the west coast of the Indian subcontinent (e.g., Suresh et al., 2013; Dhage and Strub, 2016). Future studies should identify the dominant centers of action of atmospheric forcing of intraseasonal $\zeta$ variability in the Persian Gulf, and whether coastal-trapped waves arriving in the Gulf of Oman have their origin in equatorial waves that impinged on the Maritime Continent. Our results also raise questions of whether such wave signals are felt even farther downstream along the coastal waveguide, for example, in the Red Sea. Previous investigations of sea-level variability in the Red Sea on timescales from days to decades largely emphasize the role of more local forcing (Abdelrahman, 1997; Churchill et al., 2018; Cromwell and Smeed, 1998; Osman, 1984; Patzert, 1974; Sofianos and Johns, 2001; Sultan and Elghribi 2003; Sultan et al., 1995b, 1995c, 1996). However, recent work by Alawad et al. (2017, 2019) suggests that mean sea-level variability in the Red Sea is partly related to large-scale modes of climate variability. These authors reason that this relationship is mediated by westward propagation of off-equatorial Rossby waves originating in the eastern tropical Indian Ocean. Based on our results, we hypothesize that coastal-wave propagation may also play a role in facilitating this relationship between sea level in the Red Sea and large-scale climate. We leave it to future studies to test this hypothesis.

*Acknowledgments.* The authors acknowledge support from NASA through the Sea Level Change Team (grant 80NSSC20K1241) and GRACE Follow-On Science Team (grant 80NSSC20K0728). The authors appreciate comments from two anonymous reviewers that improved the manuscript.

*Data availability statement.* Data are available through links provided in Table 1. Matlab codes used for processing the data and producing the results are available from the corresponding author upon request.

# APPENDIX

## Transport variation through the Strait of Hormuz

Insights onto the local and nonlocal forcing of transport variability through the Strait of Hormuz are given by our model. Substituting Eq. (3) for $\overline{\zeta}_t$ in Eq. (1), and assuming plane-wave solutions, we obtain after rearranging and collecting terms,

$$vWH = -i\omega S\left[\zeta_0 + \frac{L}{\rho g H}\tau - \frac{i}{\omega}\overline{q} - \frac{\overline{p}}{\rho g}\right] \Big/ \left[1 - \frac{\omega^2}{\sigma^2} - i\frac{\lambda\omega}{\sigma^2}\right], \tag{A1}$$

or, equivalently,

$$vWH = \tilde{z}_{\zeta_0}\exp\left(i\tilde{\theta}_{\zeta_0}\right)\zeta_0 + \tilde{z}_\tau \exp\left(i\tilde{\theta}_\tau\right)\tau + \tilde{z}_{\overline{q}}\exp\left(i\tilde{\theta}_{\overline{q}}\right)\overline{q} + \tilde{z}_{\overline{p}}\exp\left(i\tilde{\theta}_{\overline{p}}\right)\overline{p}, \tag{A2}$$

where

$$\tilde{\theta}_{\zeta_0} \doteq \arctan\left(\frac{\omega^2 - \sigma^2}{\lambda\omega}\right), \tag{A3}$$

$$\tilde{z}_{\zeta_0} \doteq \omega S\left[\left(1 - \frac{\omega^2}{\sigma^2}\right)^2 + \left(\frac{\lambda\omega}{\sigma^2}\right)^2\right]^{-1/2}, \tag{A4}$$

$$\tilde{\theta}_\tau \doteq \arctan\left(\frac{\omega^2 - \sigma^2}{\lambda\omega}\right), \tag{A5}$$

$$\tilde{z}_\tau \doteq \omega S\left[\left(1 - \frac{\omega^2}{\sigma^2}\right)^2 + \left(\frac{\lambda\omega}{\sigma^2}\right)^2\right]^{-1/2}\left(\frac{L}{\rho g H}\right), \tag{A6}$$

$$\tilde{\theta}_{\overline{q}} \doteq \arctan\left(\frac{\lambda\omega}{\sigma^2 - \omega^2}\right), \tag{A7}$$

$$\tilde{z}_{\overline{q}} \doteq S\left[\left(1 - \frac{\omega^2}{\sigma^2}\right)^2 + \left(\frac{\lambda\omega}{\sigma^2}\right)^2\right]^{-1/2}, \tag{A8}$$

$$\tilde{\theta}_{\overline{p}} \doteq \arctan\left(\frac{\omega^2 - \sigma^2}{\lambda\omega}\right), \tag{A9}$$

$$\tilde{z}_{\overline{p}} \doteq \frac{\omega S}{\rho g}\left[\left(1 - \frac{\omega^2}{\sigma^2}\right)^2 + \left(\frac{\lambda\omega}{\sigma^2}\right)^2\right]^{-1/2}. \tag{A10}$$

To quantify the relative roles of the different surface and boundary forcing terms on transport as a function of timescale, we multiply the frequency-dependent scaling coefficients [$\tilde{z}_j$ in Eqs. (A4), (A6), (A8), (A10)] by the same forcing fluctuations that we used earlier in section 4.b and Figure 7 ($|\zeta_0| = 2$ cm, $|\tau| = 0.005$ N m$^{-2}$, $|\overline{q}| = 1 \times 10^{-8}$ m s$^{-1}$, $|\overline{p}| = 0.5$ hPa). Results are shown in Figure A1. Resonant responses to $\zeta_0$, $\tau$, and $\overline{p}$ are seen near the Helmholtz period $2\pi/\sigma \sim 4$ d, when maximum values ($\sigma^2 S|\zeta_0|/\lambda$, $\sigma^2 SL|\tau|/\lambda\rho g H$, and $\sigma^2 S|\overline{p}|/\lambda\rho g$, respectively) are achieved.

At periods shorter (longer) than $2\pi/\sigma$, the transport response to $\zeta_0$, $\tau$, and $\overline{p}$ grows (decays) with period, such that $vWH \to 0$ as $\omega \to 0$. In contrast, the transport response to $\overline{q}$ increases universally with period, approaching the asymptotic limit $vWH \to S\overline{q}$ as $\omega \to 0$.

Given the amplitudes of the forcings, transport variations are predominantly driven by $\zeta_0$ and $\overline{q}$ on intraseasonal timescales. At longer timescales, forcing by $\overline{q}$ dominates, whereas $\zeta_0$, $\tau$, and $\overline{p}$ are more important drivers at shorter timescales. At all timescales, transport variations owing to local $\tau$ and $\overline{p}$ forcing are $\sim 1/3$ and $\sim 1/4$ as large, respectively, as transport variations due to nonlocal $\zeta_0$ forcing. This analytical exercise suggests that the intraseasonal transport variations through the Strait of Hormuz, estimated in the Discussion, mainly reflect a combination of local $\overline{q}$ and nonlocal $\zeta_0$ forcing effects.

As discussed earlier, these results are a function of the forcing scales, details of friction, and the geometry of the region, and the various forcings could be more or less important if these parameters were different (e.g., for a different marginal sea).

## References


Abdelrahman, S. M., 1997: Seasonal Fluctuations of Mean Sea Level at Gizan, Red Sea. *Journal of Coastal Research*, *13*(4), 1166–1172,

Ablain, M., A. Cazenave, G. Larnicol, M. Balmaseda, P. Cipollini, Y. Faugère, M. J. Fernandes, O. Henry, J. A. Johannessen, P. Knudsen, O. Andersen, J. Legeais, B. Meyssignac, N. Picot, M. Roca, S. Rudenko, M. G. Scharffenberg, D. Stammer, G. Timms, and J. Benveniste, 2015: Improved sea level record over the satellite altimetry era (1993–2010) from the Climate Change Initiative project. *Ocean Science*, *11*, 67–82, https://doi.org/10.5194/os-11-67-2015.

Adhikari, S., E. R. Ivins, T. Frederikse, F. W. Landerer, and L. Caron, 2019: Sea-level fingerprints emergent from GRACE mission data. *Earth System Science Data*, *11*, 629–646, https://doi.org/10.5194/essd-11-629-2019.

Adler, R. F., G. J. Huffman, A. Chang, R. Ferraro, P. Xie, J. Janowiak, B. Rudolf, U. Schneider, S. Curtis, D. Bolvin, A. Gruber, J. Susskind, and P. Arkin, 2003: The Version 2 Global Precipitation Climatology Project (GPCP) Monthly Precipitation Analysis (1979-Present). *Journal of Hydrometeorology*, *4*,1147–1167, https://doi.org/10.1175/1525-7541(2003)004<1147:TVGPCP>2.0.CO;2

Ahmad, F., and S. A. R. Sultan, 1991: Annual mean surface heat fluxes in the Arabian Gulf and the net heat transport through the Strait of Hormuz. *Atmosphere-Ocean*, *29*(1), 54–61, https://doi.org/10.1080/07055900.1991.9649392

al-Chalabi, I., 2007: Oil. The Geopolitics of Oil and Iraq. *New England Journal of Public Policy*, *21*(2), 136–139, https://scholarworks.umb.edu/nejpp/vol21/iss2/13.

Al-Jeneid, S., Bahnassy, M., Nasr, S., and El Raey, M., 2008: Vulnerability assessment and adaptation to the impacts of sea level rise on the Kingdom of Bahrain. *Mitigation and Adaptation Strategies for Global Change*, *13*, 87–104, https://doi.org/10.1007/s11027-007-9083-8.

Al-Subhi, A. M., 2010: Tide and sea level characteristics at Juaymah, west coast of the Arabian Gulf. *Journal of King Abdulaziz University Marine Science*, *21*(1), 133–149, https://doi.org/10.4197/mar.21-1.8.

Alawad, K. a. I., A. M. Al-Subhi, M. A. Alsaafani, and T. M. Alraddadi, 2017: Signatures of Tropical climate modes on the Red Sea and Gulf of Aden Sea Level. *Indian Journal of Geo Marine Sciences*, *46*(10), 2088–2096, http://nopr.niscair.res.in/handle/123456789/42751.

Alawad, K. a. I., A. M. Al-Subhi, M. A. Alsaafani, M. Ionita, and G. Lohmann, 2019: Large-Scale Mode Impacts on the Sea Level over the Red Sea and Gulf of Aden. *Remote Sensing*, *11*, 2244, https://doi.org/10.3390/rs11192224.

Alothman, A. O., M. S. Bos, R. M. S. Fernandes, and M. E. Ayhan, 2014: Sea level rise in the north-western part of the Arabian Gulf. *Journal of Geodynamics*, *81*, 105–110, https://doi.org/10.1016/j.jog.2014.09.002.

Amin, A., and K. Bankher, 1997: Causes of land subsidence in the Kingdom of Saudi Arabia. *Natural Hazards*, *16*(1), 57–63, https://doi.org/10.1023/A:1007942021332.

Ayhan, M. E., 2020: Dynamic harmonic regression modeling for monthly mean sea levels at tide gauges within the Arabian Gulf. *Journal of Geodesy*, *94*(46), https://doi.org/10.1007/s00190-020-01371-x.

Barnes, J., and A. M. Jaffe, 2006: The Persian Gulf and the Geopolitics of Oil. *Survival: Global Politics and Strategy*, *48*(1), 143–162, https://doi.org/10.1080/00396330600594348.

Barzandeh, A., N. Eshghi, F. Hosseinibalam, and S. Hassanzadeh, 2018: Wind-driven coastal upwelling along the northern shoreline of the Persian Gulf. *Bollettino di Geofisica Teorica ed Applicata*, *59*(3), 301–302, https://doi.org/10.4430/bgta0235.

Bingham, R. J., and C. W. Hughes, 2008: The relationship between sea-level and bottom pressure variability in an eddy permitting ocean model. *Geophysical Research Letters*, *35*, L03602, https://doi.org/10.1029/2007GL032662.

Burgos, A. G., B. D. Hamlington, P. R. Thompson, and R. D. Ray: Future Nuisance Flooding in Norfolk, VA, From Astronomical Tides and Annual to Decadal Internal Climate Variability. *Geophysical Research Letters*, *45*, 12432–12439, https://doi.org/10.1029/2018GL079572.

Cabanes, C., T. Huck, and A. Colin de Verdière, 2006: Contributions of Wind Forcing and Surface Heating to Interannual Sea Level Variations in the Atlantic Ocean. *Journal of Physical Oceanography*, *36*, 1739–1750.

Carrère, L., and F. Lyard, 2003: Modeling the barotropic response of the global ocean to atmospheric wind and pressure forcing—comparisons with observations. *Geophysical Research Letters*, *30*(6), 1275, https://doi.org/10.1029/2002GL016473.

Carrère, L., Y. Faugère, and M. Ablain, 2016: Major improvement of altimetry sea level estimations using pressure-derived corrections based on ERA-Interim atmospheric reanlaysis. *Ocean Science*, *12*, 825–842, https://doi.org/10.5194/os-12-825-2016.

Chao, S.-Y., T. W. Kao, and K. R. Al-Hajri, 1992: A numerical investigation of the circulation in the Arabian Gulf. *Journal of Geophysical Research*, *97*(C7), 11219–11236. https://doi.org/10.1029/92JC00841.

Cheng, X., S.-P. Xie, J. P. McCreary, Y. Qi, Y., and Y. Du, 2013: Intraseasonal variability of sea surface height in the Bay of Bengal. *Journal of Geophysical Research Oceans*, *118*(2), 816–430, https://doi.org/10.1002/jgrc.20075.

Churchill, J. H., Abualnaja, Y., Limeburner, R., and Nellayaputhenpeedika, M., 2018: The dynamics of weather-band sea level variations in the Red Sea. *Regional Studies in Marine Science*, *24*, 336–342, https://doi.org/10.1016/j.rsma.2018.09.006.

Cromwell, D., and Smeed, D. A., 1998: Altimetric observations of sea level cycles near the Strait of Bab al Mandab. *International Journal of Remote Sensing*, *19*(8), 1561–1578, https://doi.org/10.1080/014311698215351.

Dangendorf, S., A. Arns, J. G. Pinto, P. Ludwig, and J. Jensen, 2016: The exceptional influence of storm ‘Xaver’ on design water levels in the German Bight. *Environmental Research Letters*, *11*, 054001, https://doi.org/10.1088/1748-9326/11/5/054001.

Dangendorf, S., C. Hay, F. M. Calafat, M. Marcos, C. G. Piecuch, K. Berk, and J. Jensen, 2019: Persistent acceleration in global sea-level rise since the 1960s. *Nature Climate Change*, *9*, 705–710, https://doi.org/10.1038/s41558-019-0531-8.

Dee, D. P., S. M. Uppala, A. J. Simmons, P. Berrisford, P. Poli, S. Kobayashi, U. Andrae, M. A. Balmaseda, G. Balsamo, P. Bauer, P. Bechtold, A. C. M. Beljaars, L. van de Berg, J. Bidlot, N. Bormann, C. Delsol, R. Dragani, M. Fuentes, A. J. Geer, L. Haimberger, S. B. Healy, H. Hersbach, E. V. Hólm, L. Isaksen, P. Kållberg, M. Köhler, M. Matricardi, A. P. McNally, B. M. Monge-Sanz, J.-J. Morcrette, B.-K. Park, C. Peubey, P. de Rosnay, C. Tavolato, J.-N. Thépaut, and F. Vitart, 2011: The ERA-Interim reanalysis: configuration and performance of the data assimilation system. *Quarterly Journal of the Royal Meteorological Society*, **137**, 553–597, https://doi.org/10.1002/qj.828.

Dhage, L., and P. T. Strub, 2016: Intra-seasonal sea level variability along the west coast of India. *Journal of Geophysical Research Oceans*, *121*, 8172–8188, https://doi.org/10.1002/2016JC011904.

Efron, B., and T. Hastie, 2016: *Computer Age Statistical Inference: Algorithms, Evidence, and Data Science*, Cambridge University Press, 495 pp.

El-Gindy, A. A. H., 1991: Sea level variations and their relations to the meteorological factors in the Arab Gulf area with stress on monthly means. *International Hydrographic Review*, *68*(1), 109–125.

El-Gindy, A. A., and F. M. Eid, 1997: The seasonal variations of sea level due to density variations in the Arabian Gulf and Gulf of Oman. *Pakistan Journal of Marine Sciences*, *6*(1–2), 1–12.

Emery, K. O., 1956: Sediments and water in the Persian Gulf. *Bulletin of the American Association of Petroleum Geologists*, *40*(10), 2354–2383, https://doi.org/10.1306/5CEAE595-16BB-11D7-8645000102C1865D.

Feng, W., M. Zhong, and H. Z. Xu, 2012: Sea level variations in the South China Sea inferred from satellite gravimetry, altimetry, and oceanographic data. *Science in China Series D*, *55*, 10, 1696–1701, https://doi.org/10.1007/s11430-012-4394-3.

Feng, W., J.-M. Lemoine, M. Zhong, M., and H. T. Hsu, 2014: Mass-induced sea level variations in the Red Sea from GRACE, steric-corrected altimetry, in situ bottom pressure records, and hydrographic observations. *Journal of Geodynamics*, *78*, 1–7. http://dx.doi.org/10.1016/j.jog.2014.04.008.

Fenoglio-Marc, L., J. Kusche, and M. Becker, 2006: Mass variation in the Mediterranean Sea from GRACE and its validation by altimetry, steric and hydrologic fields. *Geophysical Research Letters*, *33*(L19606), https://doi.org/10.1029/2006GL026851.

Fenoglio-Marc, L., R. Rietbroek, S. Grayek, M. Becker, J. Kusche, and E. Stanev, 2012: Water mass variation in the Mediterranean and Black Seas. *Journal of Geodynamics*, *59–60*, https://doi.org/10.1016/j.jog.2012.04.001.

Frederikse, T., F. Landerer, L. Caron, S. Adhikari, D. Parkes, V. W. Humphrey, S. Dangendorf, P. Hogarth, L. Zanna, L. Cheng, and Y.-H. Wu: The causes of sea-level rise since 1900. *Nature*, *584*, 393–397, https://doi.org/10.1038/s41586-020-2591-3.

Gill, A. E., 1982: *Atmosphere-Ocean Dynamics*, Academic Press, 680 pp.

Gill, A. E., and P. P. Niiler, 1973: The theory of the seasonal variability in the ocean. *Deep-Sea Research*, *20*, 141–177, https://doi.org/10.1016/0011-7471(73)90049-1.

Good, S. A., M. J. Martin, and N. A. Rayner, 2013: EN4: Quality controlled ocean temperature and salinity profiles and monthly objective analyses with uncertainty estimates. *Journal of Geophysical Research*, *118*, 6704–6716, https://doi.org/10.1002/2013JC009067.

Gregory, J. M., S. M. Griffies, C. W. Hughes, J. A. Lowe, J. A. Church, I. Fukumori, N. Gomez, R. E. Kopp, F. Landerer, G. Le Cozannet, R. M. Ponte, D. Stammer, M. E. Tamisiea, and R. S. W. van de Wal, 2019: Concepts and Terminology for Sea Level: Mean, Variability and Change, Both Local and Global. *Surveys in Geophysics*, *40*, 1251–1289, https://doi.org/10.1007/s10712-019-09525-z.

Hassanzadeh, S., A. Kiasatpour, and F. Hosseinibalam, 2007: Sea-level response to atmospheric forcing along the north coast of Persian Gulf. *Meteorology and Atmospheric Physics*, *95*, 223–237, https://doi.org/10.1007/s00703-006-0213-8.

Hirose, N., I. Fukumori, V. Zlotnicki, and R. M. Ponte, 2001: Modeling the high-frequency barotropic response of the ocean to atmospheric disturbances: Sensitivity to forcing, topography, and friction. *Journal of Geophysical Research*, *106*(C12), 30987–30995, https://doi.org/10.1029/2000JC000763.

Holgate, S. J., A. Matthews, P. L. Woodworth, L. J. Rickards, M. E. Tamisiea, E. Bradshaw, P. R. Foden, K. M. Gordon, S. Jevrejeva, and J. Pugh, 2013: New Data Systems and Products and the Permanent Service for Mean Sea Level. *Journal of Coastal Research*, *29*(3), 493–504, https://doi.org/10.2112/JCOASTRES-D-12-00175.1.

Hosseinibalam, F., S. Hassanzadeh, and A. Kiasatpour, 2007: Interannual variability and seasonal contribution of thermal expansion to sea level in the Persian Gulf. *Deep-Sea Research Part I*, *54*, 1474–1485, https://doi.org/10.1016/j.dsr.2007.05.005.

Hughes, C. W., I. Fukumori, S. M. Griffies, J. M. Huthnance, S. Minobe, P. Spence, K. R. Thompson, and A. Wise, 2019: Sea Level and the Role of Coastal Trapped Waves in Mediating the Influence of the Open Ocean on the Coast. *Surveys in Geophysics*, *40*, 1467–1492, https://doi.org/10.1007/s10712-019-09535-x.

Iskandar, I., W. Mardiansyah, Y. Masumoto, and T. Yamagata, 2005: Intraseasonal Kelvin waves along the southern coast of Sumatra and Java. *Journal of Geophysical Research*, *110*(C04013), https://doi.org/10.1029/2004JC002508.

Johns, W. E., G. A. Jacobs, J. C. Kindle, S. P. Murray, and M. Carron, 1999: Arabian Marginal Seas and Gulfs: report of a workshop held at Stennis Space Center, Miss., 11–13 May 1999. University of Miami RSMAS Technical Report 2000-01, 60 pp.

Johns, W. E., F. Yao, D. B. Olson, S. A. Josey, J. P. Grist, and D. A. Smeed, 2003: Observations of seasonal exchange through the Straits of Hormuz and the inferred heat and freshwater budgets of the Persian Gulf. *Journal of Geophysical Research*, *108*(C12), 3991, https://doi.org/10.1029/2003JC001881.

Kämpf, J., and M. Sadrinasab, 2006: The circulation of the Persian Gulf: a numerical study. *Ocean Science*, *2*, 27–41, https://doi.org/10.5194/os-2-27-2006.

Kopp, R. E., R. M. Horton, C. M. Little, J. X. Mitrovica, M. Oppenheimer, D. J. Rasmussen, B. H. Strauss, and C. Tebaldi, 2014: Probabilistic 21st and 22nd century sea-level projections at a global network of tide-gauge sites. *Earth's Future*, *2*, 383–406, https://doi.org/10.1002/2014EF000239.

Kopp, R. E., R. M. DeConto, D. A. Bader, C. C. Hay, R. M. Horton, S. Kulp, M. Oppenheimer, D. Pollard, and B. H. Strauss, 2017: Evolving Understanding of Antarctic Ice-Sheet Physics and Ambiguity in Probabilistic Sea-Level Projections. *Earth's Future*, *5*, 1217–1233, https://doi.org/10.1002/2017EF000663.

Lafta, A. A., S. A. Altaei, and N. H. Al-Hashimi, 2020: Impacts of potential sea-level rise on tidal dynamics in Khor Abdullah and Khor Al-Zubair, northwest of Arabian Gulf. *Earth Systems and Environment*, *4*, 93–105, https://doi.org/10.1007/s41748-020-00147-9.

Landerer, F. W., and D. L. Volkov, 2013: The anatomy of recent large sea level fluctuations in the Mediterranean Sea. *Geophysical Research Letters*, *40*, 553–557, https://doi.org/10.1002/grl.50140.

Landerer, F. W., F. M. Flechtner, H. Save, F. H. Webb, T. Bandikova, W. I. Bertiger, S. V. Bettadpur, S. H. Byun, C. Dahle, H. Dobslaw, E. Fahnestock, N. Harvey, Z. Kang, G. L. H. Kruizinga, B. D. Loomis, C. McCullough, M. Murböck, P. Nagel, M. Paik, N. Pie, S. Poole, D. Strekalov, M. E. Tamisiea, F. Wang, M. M. Watkins, H.-Y. Wen, D. N. Wiese, and D.-N. Yuan, 2020: Extending the Global Mass Change Data Record: GRACE Follow?On Instrument and Science Data Performance. *Geophysical Research Letters*, *47*(12), e2020GL088306, https://doi.org/10.1029/2020GL088306.

Large, W. G., and S. G. Yeager, 2004: Diurnal to Decadal Global Forcing For Ocean and Sea-Ice Models: The Data Sets and Flux Climatologies. NCAR/TN-460+ STR, NCAR Technical Note, 112 pp.

Larson, A., 2007: Oil. The Geopolitics of Oil and Natural Gass. *New England Journal of Public Policy*, *21*(2), 215–219, https://scholarworks.umb.edu/nejpp/vol21/iss2/18.

Legeais, J.-F., M. Ablain, L. Zawadzki, H. Zuo, J. A. Johannessen, M. G. Scharffenberg, L. Fenoglio-Marc, M. J. Fernandes, O. B. Andersen, S. Rudenko, P. Cipollini, G. D. Quartly, M. Passaro, A. Cazenave, and J. Benveniste, 2017.: An improved and homogeneous altimeter sea level record from the ESA Climate Change Initiative. *Earth System Science Data*, *10*, 281–301, https://doi.org/10.5194/essd-10-281-2018.

Long, X., M. J. Widlansky, F. Schloesser, P. R. Thompson, H. Annamalai, M. A. Merrifield, and H. Yoon, 2020: Higher Sea Levels at Hawaii Caused by Strong El Niño and Weak Trade Winds. *Journal of Climate*, *33*, 3037–3059, https://doi.org/10.1175/JCLI-D-19-0221.1.

Loomis, B. D., and S. B. Luthcke, 2017: Mass evolution of Mediterranean, Black, Red, and Caspian Seas from GRACE and altimetry: accuracy assessment and solution calibration. *Journal of Geodesy*, *91*, 195–206, https://doi.org/10.1007/s00190-016-0952-3.

Mathers, E. L., and P. L. Woodworth, 2001: Departures from the local inverse barometer model observed in altimeter and tide gauge data and in a global barotropic numerical model. *Journal of Geophysical Research*, *106*(C4), 9657–6972, https://doi.org/10.1029/2000JC000241.

Mathers, E. L., and P. L. Woodworth, 2004: A study of departures from the inverse-barometer response of sea level to air-pressure forcing at a period of 5 days. *Quarterly Journal of the Royal Meteorological Society*, *130*, 725–738, https://doi.org/10.1256/qj.03.46.

Meyssignac, B., C. G. Piecuch, C. J. Merchant, M.-F. Racault, H. Palanisamy, C. MacIntosh, S. Sathyendranath, and R. Brewin, 2017: Causes of the Regional Variability in Observed Sea Level, Sea Surface Temperature and Ocean Colour Over the Period 1993–2011. *Surveys in Geophysics*, *38*, 187–215, https://doi.org/10.1007/s10712-016-9383-1.

Nerem, R. S., B. D. Beckley, J. T. Fasullo, B. D. Hamlington, D. Masters, and G. T. Mitchum, 2018: Climate-change-driven accelerated sea-level rise detected in the altimeter era. *Proceedings of the National Academy of Sciences*, *115*(9), 2022–2025, https://doi.org/10.1073/pnas.1717312115 .

Oliver, E. C. J., and K. R. Thompson, 2010: Madden-Julian Oscillation and sea level: local and remote forcing. *Journal of Geophysical Research*, *115*(C01003), https://doi.org/10.1029/2009JC005337.

Osman, M. M., 1984: Variation of sea level at Port-Sudan. *International Hydrographic Review*, *61*(2).

Patzert, W. C., 1974: Wind-induced reversal in Red Sea circulation. *Deep-Sea Research*, *21*(2), 109–121, https://doi.org/10.1016/0011-7471(74)90068-0.

Permanent Service for Mean Sea Level (PSMSL), 2020: "Tide Gauge Data", Retrieved 1 Jul 2019 from http://www.psmsl.org/data/obtaining/.

Piecuch, C. G., and R. M. Ponte, 2015: A wind-driven nonseasonal barotropic fluctuation of the Canadian inland seas. *Ocean Science*, *11*, 175–185, https://doi.org/10.5194/os-11-175-2015.

Piecuch, C. G., K. Bittermann, A. C. Kemp, R. M. Ponte, C. M. Little, S. E. Engelhart, and S. J. Lentz, 2018: River-discharge effects on United States Atlantic and Gulf coast sea-level changes. *Proceedings of the National Academy of Sciences*, *115*(30), 7729–7734, https://doi.org/10.1073/pnas.1805428115.

Piecuch, C. G., Landerer, F. W., and R. M. Ponte, 2018b: Tide gauge records reveal improved processing of Gravity Recovery and Climate Experiment time-variable mass solutions over the coastal ocean. *Geophysical Journal International*, *214*, 1401–1412, https://doi.org/10.1093/gji/ggy207.

Piecuch, C. G., F. M. Calafat, S. Dangendorf, and G. Jordà, 2019: The Ability of Barotropic Models to Simulate Historical Mean Sea Level Changes from Coastal Tide Gauge Data. *Surveys in Geophysics*, *40*, 1399–1435, https://doi.org/10.1007/s10712-019-09537-9.

Ponte, R. M., 1992: The Sea Level Response of a Stratified Ocean to Barometric Pressure Forcing. *Journal of Physical Oceanography*, *22*, 109–113, https://doi.org/10.1175/1520-0485(1992)022<0109:TSLROA>2.0.CO;2.

Ponte, R. M., 1994: Understanding the relation between wind- and pressure-driven sea level variability. *Journal of Geophysical Research*, *99*(C4), 8033–8039, https://doi.org/10.1029/94JC00217.

Ponte, R. M., 2006: Oceanic Response to Surface Loading Effects Neglected in Volume-Conserving Models. *Journal of Physical Oceanography*, *36*, 426–434, https://doi.org/10.1175/JPO2843.1.

Privett, D. W., 1959: Monthly charts of evaporation from the N. Indian Ocean (including the Red Sea and the Persian Gulf). *Quarterly Journal of the Royal Meteorological Society*, *85*, 424–428, https://doi.org/10.1002/qj.49708536614.

Quartly, G. D., J.-F. Legeais, M. Ablain, L. Zawadzki, M. J. Fernandes, S. Rudenko, L. Carrère, P. N. García, P. Cipollini, O. B. Andersen, J.-C. Poisson, S. Mbajon Njiche, A. Cazenave, and J. Benveniste, 2017: A new phase in the production of quality-controlled sea level data. *Earth System Science Data*, *9*, 557–572, https://doi.org/10.5194/essd-9-557-2017.

Ray, R. D., and G. Foster, 2016: Future nuisance flooding at Boston caused by astronomical tides alone. *Earth's Future*, *4*, 578–587, https://doi.org/10.1002/2016EF000423.

Reynolds, R. M., 1993: Physical oceanography of the Gulf, Strait of Hormuz, and the Gulf of Oman–results from the *Mt Mitchell* Expedition. *Marine Pollution Bulletin*, *27*, 35–59, https://doi.org/10.1016/0025-326X(93)90007-7.

Rohith, B., A. Paul, F. Durand, L. Testut, S. Prerna, M. Afroosa, S. S. V. S. Ramkrishna, and S. S. C. Shenoi, 2019: Basin-wide sea level coherency in the tropical Indian Ocean driven by Madden-Julian Oscillation. *Nature Communications*, *10*, 1257, https://doi.org/10.1038/s41467-019-09243-5.

Sharaf El Din, S. H., 1990: Sea level variation along the western coast of the Arabian Gulf. *International Hydrographic Review*, *67*(1), 103–109.

Siddig, N. A., A. M. Al-Subhi, and M. A. Alsaafani, 2019: Tide and mean sea level trend in the west coast of the Arabian Gulf from tide gauges and multi-missions satellite altimeter. *Oceanologia*, *61*, 401–411, https://doi.org/10.1016/j.oceano.2019.05.003.

Sofianos, S. S., and Johns, W. E., 2001: Wind induced sea level variability in the Red Sea. *Geophysical Research Letters*, *28*(16), 3175–3178, https://doi.org/10.1029/2000GL012442.

Sultan, S. A. R., F. Ahmad, N. M. Elghribi, and A. M. Al-Subhi, 1995a: An analysis of Arabian Gulf mean sea level. *Continental Shelf Research*, *15*(11/12), 1471–1482, https://doi.org/10.1016/0278-4343(94)00081-W.

Sultan, S. A. R., Ahmad, F., and Elghribi, N. M., 1995b: Sea level variability in the central Red Sea. *Oceanologica Acta*, *18*(6).

Sultan, S. A. R., Ahmad, F., and El-Hassan, A., 1995c: Seasonal variations of the sea level in the central part of the Red Sea. *Estuarine, Coastal and Shelf Science*, *40*, 1–8, https://doi.org/10.1016/0272-7714(95)90008-X.

Sultan, S. A. R., Ahmad, F., and Nassar, D., 1996: Relative contribution of external sources of mean sea-level variations at Port Sudan, Red Sea. *Estuarine, Coastal and Shelf Science*, *42*, 19–30, https://doi.org/10.1006/ecss.1996.0002.

Sultan, S. A. R., M. O. Moamar, N. M. El-Ghribi, and R. Williams, 2000: Sea level changes along the Saudi coast of the Arabian Gulf. *Indian Journal of Marine Sciences*, *29*, 191–200.

Sultan, S. A. R., and Elghribi, N. M., 2003: Sea level changes in the central part of the Red Sea. *Indian Journal of Marine Sciences*, *32*(2), 114–122.

Suresh, I., J. Vialard, M. Lengaigne, W. Han, J. McCreary, F. Durand, and P. M. Muraleedharan, 2013: Origins of wind-driven intraseasonal sea level variations in the North Indian Ocean coastal waveguide. *Geophysical Research Letters*, *40*, 5740–5744, https://doi.org/10.1002/2013GL058312.

Suresh, I., Vialard, J., Izumo, T., Lengaigne, M., Han, W., McCreary, J., and Muraleedharan, P. M., 2016: Dominant role of winds near Sri Lanka in driving seasonal sea level variations along the west coast of India. *Geophysical Research Letters*, *43*, 7028–7035, https://doi.org/10.1002/2016GL069976

Sweet, W. V., M. Menendez, A. Genz, J. Obeysekera, J. Park, and J. J. Marra, 2017: In Tide's Way: Southeast Florida?s September 2015 Sunny-day Flood. *Bulletin of the American Meteorological Society*, *97*(12), S25–S30, https://doi.org/10.1175/BAMS-D-16-0117.1.

Swift, S. A., and A. S. Bower, 2003: Formation and circulation of dense water in the Persian/Arabian Gulf. *Journal of Geophysical Research*, *108*(C1), 3004, https://doi.org/10.1029/2002JC001360.

Thoppil, P. G., and P. J. Hogan, 2010: A Modeling Study of Circulation and Eddies in the Persian Gulf. *Journal of Physical Oceanography*, *40*, 2122–2134, https://doi.org/10.1175/2010JPO4227.1.

Tregoning, P., K. Lambeck, and G. Ramillien, 2008: GRACE estimates of sea surface height anomalies in the Gulf of Carpentaria, Australia. *Earth and Planetary Science Letters*, *271*, 241–244, https://doi.org/10.1016/j.epsl.2008.04.018.

Tsujino, H., S. Urakawa, H. Nakano, R. J. Small, W. M. Kim, S. G. Yeager, G. Danabasoglu, T. Suzuki, J. L. Bamber, M. Bentsen, C. W. Böning, A. Bozec, E. P. Chassignet, E. Curchitser, F. B. Dias, P. J. Durack, S. M. Griffies, Y. Harada, M. Ilicak, S. A. Josey, C. Kobayashi, S. Kobayashi, Y. Komuro, W. G. Large, J. Le Sommer, S. J. Marsland, S. Masina, M. Scheinert, H. Tomita, M. Valdivieso, and D. Yamazaki, 2018: JRA-55 based surface dataset for driving ocean?sea-ice models (JRA55-do). *Ocean Modelling*, *130*, 79–139, https://doi.org/10.1016/j.ocemod.2018.07.002.

Vinogradova, N. T., R. M. Ponte, and D. Stammer, 2007: Relation between sea level and bottom pressure and the vertical dependence of oceanic variability. *Geophysical Research Letters*, *34*, L03608, https://doi.org/10.1029/2006GL028588.

Vivier, F., K. A. Kelly, and L. Thompson, 1999: Contributions of wind forcing, waves, and surface heating to sea surface height observations in the Pacific Ocean. *Journal of Geophysical Research*, *104*(C9), 20767–20788, https://doi.org/10.1029/1999JC900096.

Volkov, D. L., W. E. Johns, and T. B. Belonenko, 2016: Dynamic response of the Black Sea elevation to intraseasonal fluctuations of the Mediterranean sea level. *Geophysical Research*

*Letters*, *43*, 283–290, https://doi.org/10.1002/ 2015GL066876.

von Storch, H., and F. W. Zwiers, 1999: *Statistical Analysis in Climate Research*, Cambridge University Press, 496 pp.

Wahr, J. W., D. A. Smeed, E. Leuliette, and S. Swenson, 2014: Seasonal variability of the Red Sea, from satellite gravimetry, radar altimetry, and in situ observations. *Journal of Geophysical Research Oceans*, *119*, 5091–5104, https://doi.org/10.1002/2014JC010161.

Waliser, D. E., R. Murtugudde, and L. E. Lucas, 2003: Indo-Pacific Ocean response to atmospheric intraseasonal variability: 1. Austral summer and the Madden-Julian Oscillation. *Journal of Geophysical Research*, *108*(C5), 3160, https://doi.org/10.1029/2002JC001620.

Waliser, D. E., R. Murtugudde, and L. E. Lucas, 2003: Indo-Pacific Ocean response to atmospheric intraseasonal variability: 2. Boreal summer and the Intraseasonal Oscillation. *Journal of Geophysical Research*, *109*(C03030), 3160, https://doi.org/10.1029/2003JC002002.

Wang, J., J. Wang, and X. Cheng, 2015: Mass-induced sea level variations in the Gulf of Carpentaria. *Journal of Oceanography*, *71*, 449–461, https://doi.org/10.1007/s10872-015-0304-6.

Watkins, M. M., D. N. Wiese, D.-H. Yuan, C. Boening, and F. W. Landerer, 2015: Improved methods for observing Earth?s time variable mass distribution with GRACE using spherical cap mascons. *Journal of Geophysical Research: Solid Earth*, *120*, 2648–2671, https://doi.org/10.1002/2014JB011547.

Wiese, D. N., F. W. Landerer, and M. M. Watkins, 2016: Quantifying and reducing leakage errors in the JPL RL05M GRACE mascon solution. *Water Resources Research*, *52*(9), 7490–7502, https://doi.org/10.1002/2016WR019344.

Wouters, B., and D. Chambers, 2010: Analysis of seasonal ocean bottom pressure variability in the Gulf of Thailand from GRACE. *Global and Planetary Change*, *74*, 76–81, https://doi.org/10.1016/j.gloplacha.2010.08.002.

Wunsch, C., and D. Stammer, 1997: Atmospheric loading and the “inverted barometer” effect. *Reviews in Geophysics*, *35*(1), 79–107, https://doi.org/10.1029/96RG03037.

Yao, F., and W. E. Johns, 2010: A HYCOM modeling study of the Persian Gulf: 1. Model configurations and surface circulation. *Journal of Geophysical Research*, *115*(C11017), https://doi.org/10.1029/2009JC005781.

Yu, L., and R. A. Weller, 2007: Objectively Analyzed Air-Sea Heat Fluxes for the Global Ice-Free Oceans (1981–2005). *Bulletin of the American Meteorological Society*, *88*(4), 527–540, https://doi.org/10.1175/BAMS-88-4-527.

# LIST OF TABLES

| Data set | Location |
|---|---|
| Altimetry | `ftp://anon-ftp.ceda.ac.uk/neodc/esacci/sea_level/data/L4/MSLA/v2.0/` |
| GRACE | `https://podaac.jpl.nasa.gov/dataset/TELLUS_GRAC-GRFO_MASCON_CRI_GRID_RL06_V2` |
| Tide gauges | `https://www.psmsl.org/data/obtaining/complete.php` |
| ERA-Interim | `http://cmip5.whoi.edu/?page_id=566` |
| GPCP | `https://psl.noaa.gov/data/gridded/data.gpcp.html` |
| OAFlux | `ftp://ftp.whoi.edu/pub/science/oaflux/data_v3/monthly/evaporation/` |
| JRA55-do | `http://amaterasu.ees.hokudai.ac.jp/~tsujino/JRA55-do-suppl/runoff/` |

TABLE 1. Data sources. All websites are current as of this writing.

| Station Name | Nation | PSMSL Identifier | Longitude (°E) | Latitude (°N) | Span | Completeness |
|---|---|---|---|---|---|---|
| Mina Sulman | Bahrain | 1494 | 50.6 | 26.2 | 1979–2006 | 66.1% |
| Emam Hassan* | Iran | 1868 | 50.3 | 29.8 | 1995–2006 | 91.7% |
| Bushehr* | Iran | 1939 | 50.8 | 28.9 | 2004–2006 | 100.0% |
| Kangan* | Iran | 1869 | 52.1 | 27.8 | 1995–2006 | 98.6% |
| Shahid Rajaee* | Iran | 1870 | 56.1 | 27.1 | 1995–2006 | 100.0% |

TABLE 2. Description of tide-gauge records. Asterisk indicates metric data without complete datum histories.

| Parameter | Description | Value |
|---|---|---|
| $\zeta$ | Ocean Dynamic Sea Level | — |
| $\tau$ | Mean Wind Stress Along Strait of Hormuz | — |
| $q$ | Surface Freshwater Flux | — |
| $p$ | Barometric Pressure | — |
| $\zeta_0$ | Ocean Dynamic Sea Level in Gulf of Oman | — |
| $\overline{\cdot}$ | Spatial Average over Persian Gulf | — |
| $S$ | Surface Area of Persian Gulf | $2.2 \times 10^5$ km$^2$ |
| $H$ | Average Depth of Persian Gulf | 30 m |
| $L$ | Length of Strait of Hormuz | 400 km |
| $W$ | Width of Strait of Hormuz | 100 km |
| $g$ | Gravitational Acceleration | 9.81 m s$^{-2}$ |
| $\rho$ | Ocean Density | 1029 kg m$^{-3}$ |
| $r$ | Friction Coefficient$^\dagger$ | $1 \times 10^{-3}$–$1 \times 10^{-2}$ m s$^{-1}$ |
| $\sigma$ | Inverse Resonance Timescale | $1.8 \times 10^{-5}$ s$^{-1}$ |
| $\lambda$ | Inverse Frictional Timescale | $3.3 \times 10^{-5}$–$3.3 \times 10^{-4}$ s$^{-1}$ |

TABLE 3. Descriptions of and, where applicable, reasonable values for variables and parameters in governing equations. $^\dagger$Values of the friction coefficient $r$ are uncertain. Previous studies variously use values ranging from as small as $4 \times 10^{-5}$ m s$^{-1}$ (e.g., Ponte, 1994) to as large as $2 \times 10^{-2}$ m s$^{-1}$ (e.g., Ponte, 2006). Values in the table represent a reasonable, physically plausible range based on choices made in previous studies.

| Parameter (Units) | Theoretical Range | Empirical Value |
| --- | --- | --- |
| $z_{\zeta_0}$ (unitless) | 0.8–1.0 | $1.0 \pm 0.2$ |
| $\theta_{\zeta_0}$ (degrees) | 5–38 | $5 \pm 10$ |
| $z_\tau$ (m Pa$^{-1}$) | 1.0–1.3 | $1.5 \pm 0.5$ |
| $\theta_\tau$ (degrees) | 5–38 | $30 \pm 25$ |
| $z_{\overline{q}}$ (days) | 1.2–9.0 | $9.4 \pm 3.7$ |
| $\theta_{\overline{q}}$ (degrees) | 3–38 | $30 \pm 27$ |
| $z_{\overline{p}}$ (cm mb$^{-1}$) | 0.1–0.5 | $0.8 \pm 0.5$ |
| $\theta_{\overline{p}}$ (degrees) | 56–87 | $65 \pm 52$ |

TABLE 4. Estimates of the scaling coefficients ($z_j$) and phase angles ($\theta_j$) in Eq. (4). The theoretical ranges are determined by averaging Eqs. (5)–(12) over the range $\omega = 2\pi \big/ (6 \text{ months})$ to $2\pi \big/ (2 \text{ months})$ using the constant values for $\sigma$, $L$, $\rho$, $g$, and $H$ and the minimum and maximum values for $\lambda$ tabulated in Table 3. Empirical values are determined through multiple linear regression involving $\overline{\zeta}$ and $\zeta_0$ from altimetry, $\tau$ and $\overline{p}$ from ERA-Interim, and $\overline{q}$ based on JRA55-do, GPCP, and OAFlux, and are presented as 95% confidence intervals estimated based on bootstrapping. Scaling coefficients are given to one decimal point and phase angles are rounded to the nearest degree.

# LIST OF FIGURES

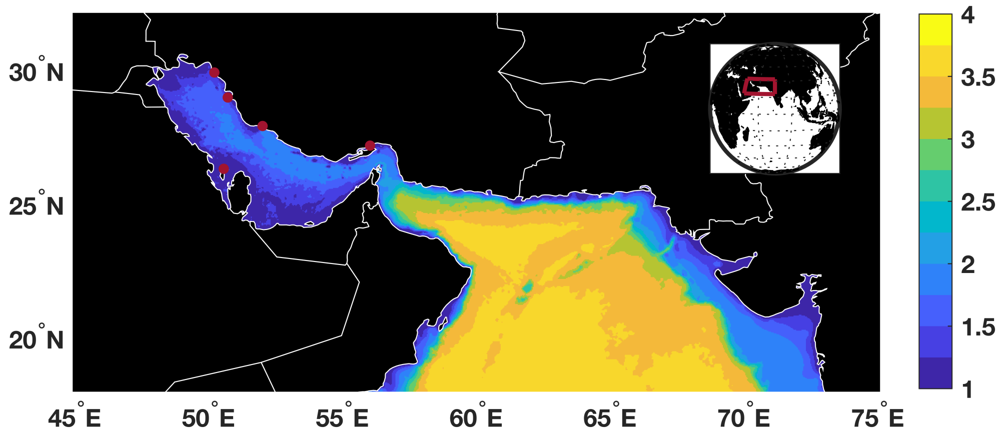


FIG. 1. Study area. White lines indicate national boundaries. Color shading identifies ocean depth. (Note the logarithmic scale bar and units of $\log_{10}$ m.) Red dots denote locations of tide gauges (Table 2). Inset shows the study area in a global context.

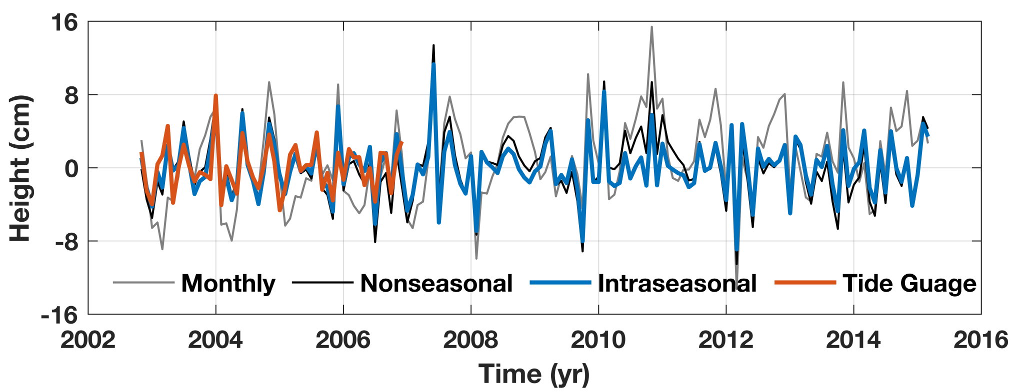


Fig. 2. Monthly ocean dynamic sea level in the Persian Gulf between November 2002 and March 2015 from satellite altimetry (gray, black, blue) and tide gauges (oranges). The satellite-altimetry data are spatially averaged over the Persian Gulf whereas the tide-gauge data represent a composite average over five sites (Figure 1). The raw monthly altimetry data are shown in gray, whereas the black and blue indicate the altimetry data with filtering applied to isolate nonseasonal and intraseasonal timescales, respectively. The tide-gauge data (orange) have been filtered to isolate intraseasonal periods and adjusted for the inverted-barometer effect. The standard deviations of the gray, black, blue, and orange time series are 4.7, 3.5, 3.0, and 2.5 cm, respectively.

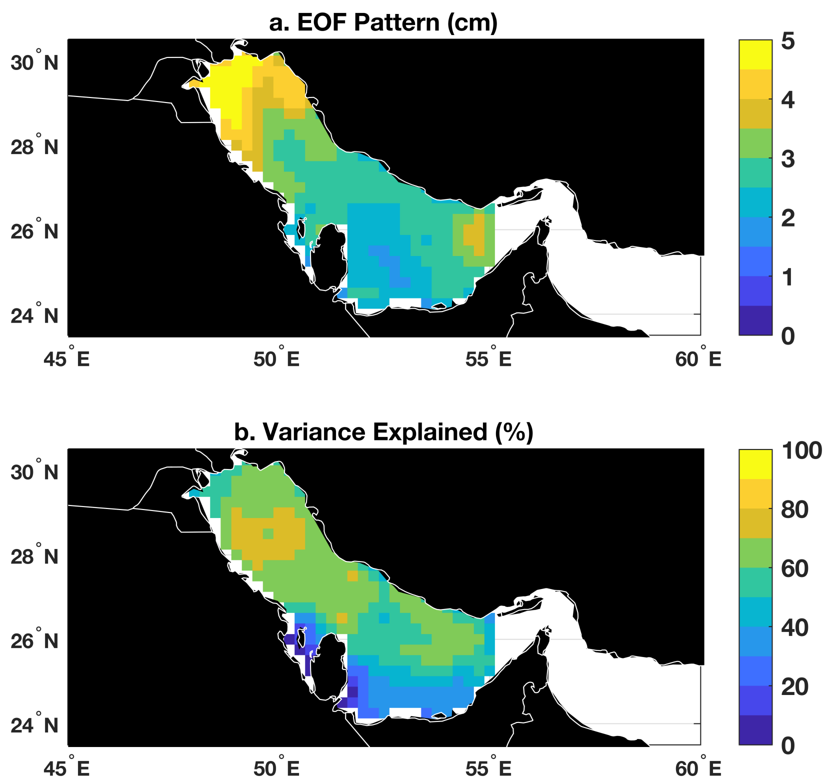


FIG. 3. **(a.)** Spatial pattern (eigenvector) of the first $\zeta$ EOF mode across the Persian Gulf from intraseasonal altimetry data. Units are cm. **(b.)** Local $\zeta$ variance explained by the first EOF mode. Units are percent of total variance.

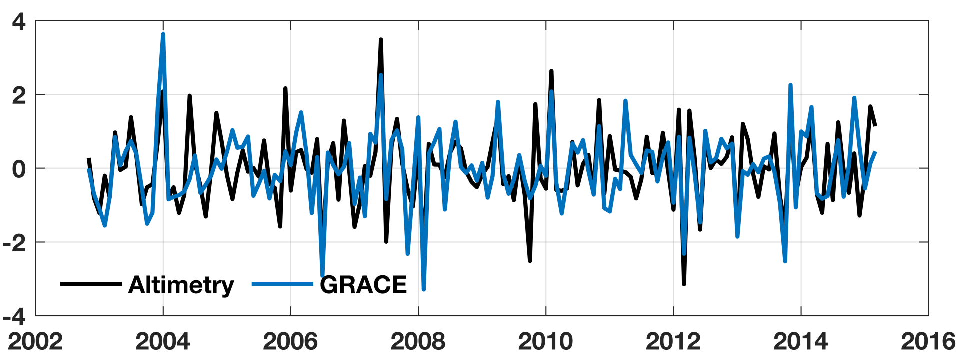


FIG. 4. Principal-component time series of the first EOF modes from altimetry $\zeta$ (black) and GRACE $R_m$ (blue) over the Persian Gulf. Time series have been normalized to unit variance (physical units are shown for the eigenvectors in Figures 3 and 5).

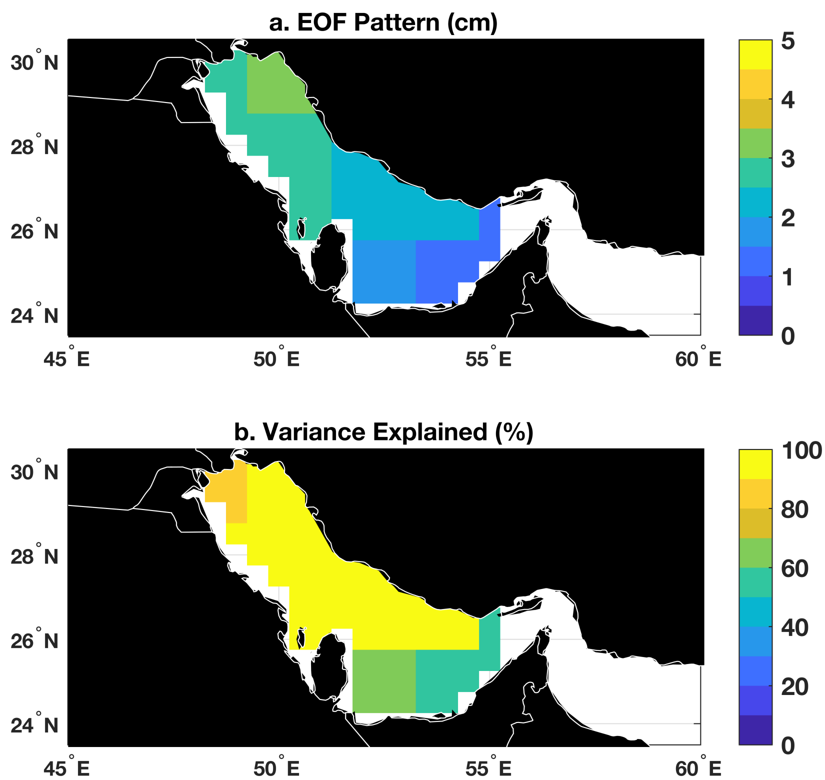


FIG. 5. **(a.)** Spatial pattern (eigenvector) of the first $R_m$ EOF mode across the Persian Gulf from intraseasonal GRACE data. Units are cm. **(b.)** Local $R_m$ variance explained by the first EOF mode. Units are percent of total variance.

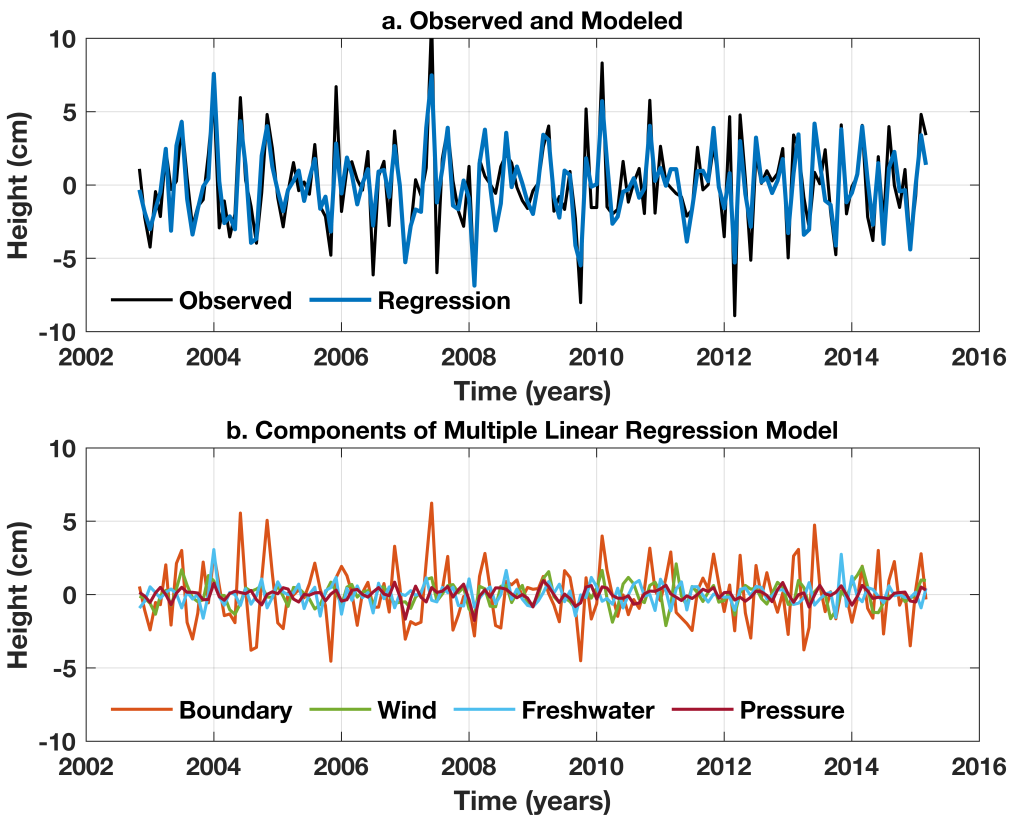


FIG. 6. **(a.)** Time series of intraseasonal $\overline{\zeta}$ from satellite altimetry (black) and the results of the multiple linear regression model (blue). Units are cm. **(b.)** Breakdown of contributors to regression model—boundary forcing $\zeta_0$ (orange), wind stress $\tau$ (green), freshwater flux $\overline{q}$ (blue), and barometric pressure $\overline{p}$ (red). Units are cm.

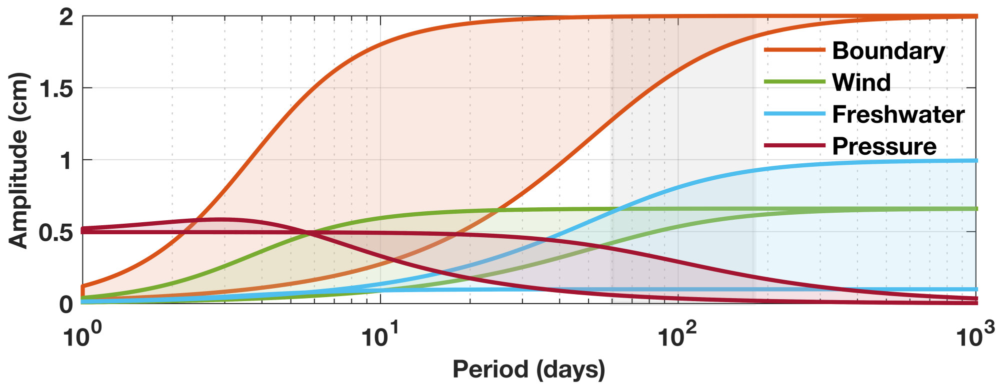


FIG. 7. Amplitude of $\overline{\zeta}$ response to boundary forcing $\zeta_0$ (orange), wind stress $\tau$ (green), freshwater flux $\overline{q}$ (blue), and barometric pressure $\overline{p}$ (red) as a function of period. Values are based on Eqs. (6), (8), (10), (12) using parameter values from Table 3. Upper and lower lines are bounds determined by the range of friction coefficient $r$. See text for more details. Gray shading indicates intraseasonal periods of primary interest here.

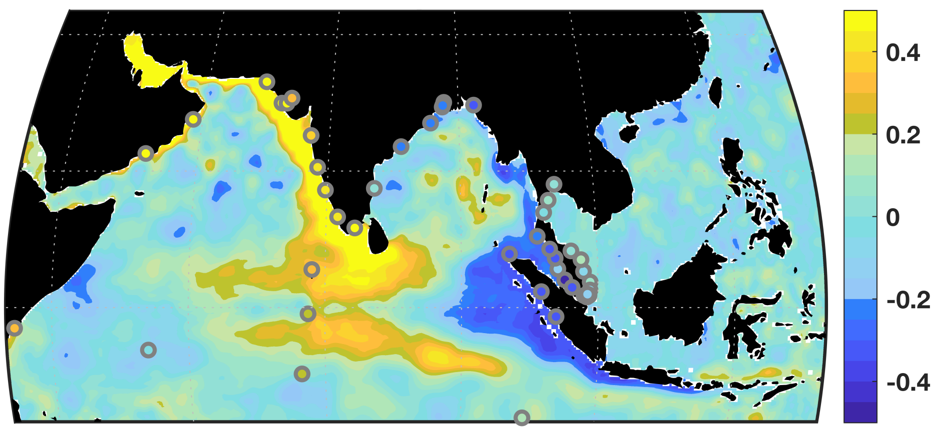


FIG. 8. Shading represents correlation coefficients between Gulf of Oman $\zeta_0$ and $\zeta$ from altimetry over the Equatorial and North Indian Ocean. Dots are the same, but based on $\zeta$ from available tide gauges. Light shading indicates values that are not distinguishable from zero at the 95% confidence level (assuming 100 degrees of freedom).

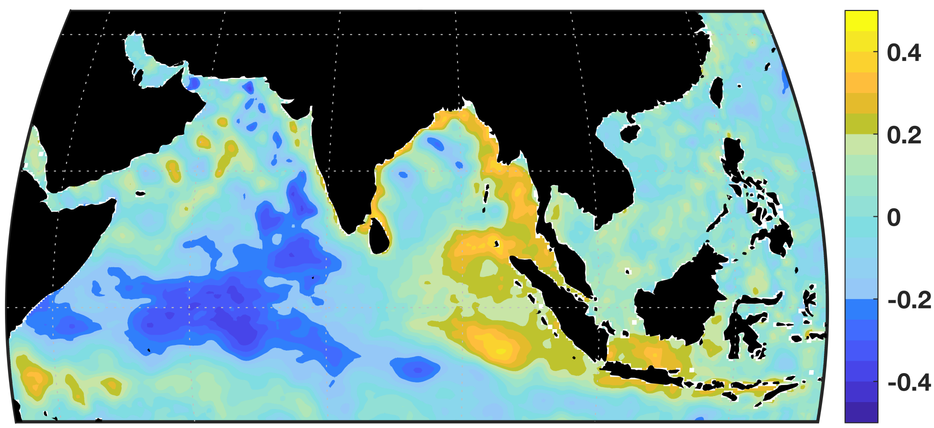


1082 Fig. 9. Shading represents correlation coefficients between Gulf of Oman $\zeta_0$ and $\mathcal{H}(\zeta)$ from altimetry over
1083 the Equatorial and North Indian Ocean. Light shading indicates values that are not distinguishable from zero at
1084 the 95% confidence level (assuming 100 degrees of freedom).

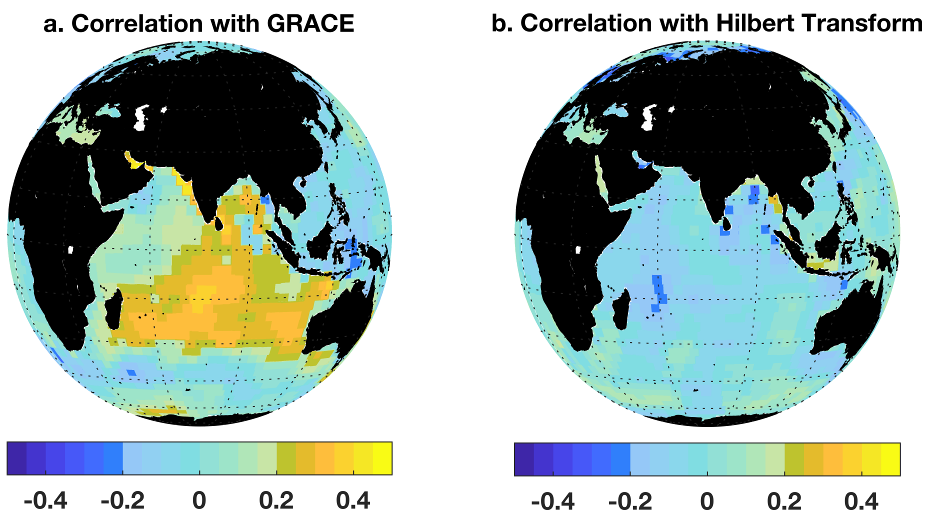


FIG. 10. Correlation coefficient between Gulf of Oman $\zeta_0$ and either **(a.)** $R_m$ from GRACE or **(b.)** $\mathcal{H}(R_m)$ over the Indian Ocean. Light shading indicates values that are not distinguishable from zero at the 95% confidence level (assuming 100 degrees of freedom).

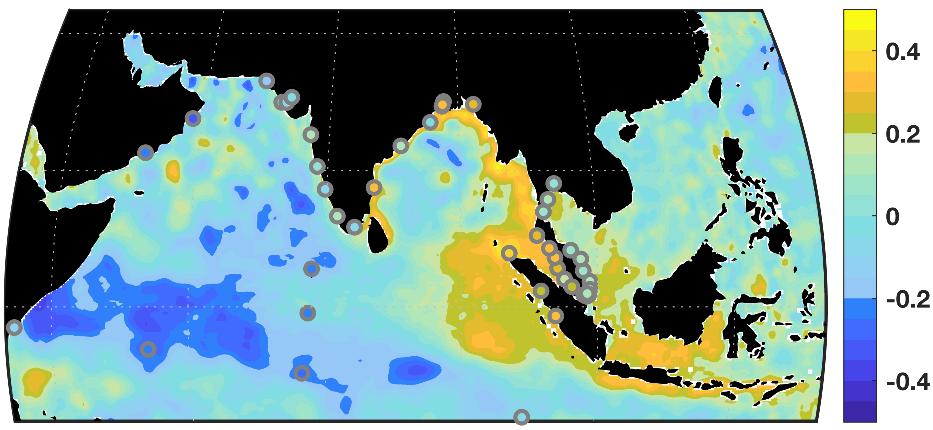


1088 FIG. 11. Shading represents correlation coefficients between Gulf of Oman $\zeta_0$ and altimetric $\zeta$ elsewhere over the Equatorial and North Indian Ocean 1 month earlier (i.e., $\zeta_0$ is lagging $\zeta$ elsewhere). Dots are the same, but based on $\zeta$ from available tide gauges. Light shading indicates values that are not distinguishable from zero at the 95% confidence level (assuming 100 degrees of freedom).

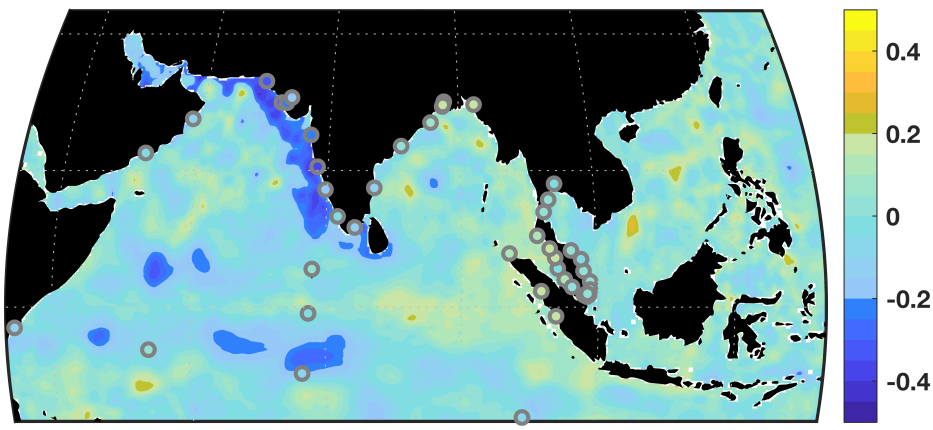


1092 FIG. 12. Shading represents correlation coefficients between Gulf of Oman $\zeta_0$ and altimetric $\zeta$ elsewhere over
1093 the Equatorial and North Indian Ocean 2 months earlier (i.e., $\zeta_0$ is lagging $\zeta$ elsewhere). Dots are the same, but
1094 based on $\zeta$ from available tide gauges. Light shading indicates values that are not distinguishable from zero at
1095 the 95% confidence level (assuming 100 degrees of freedom).

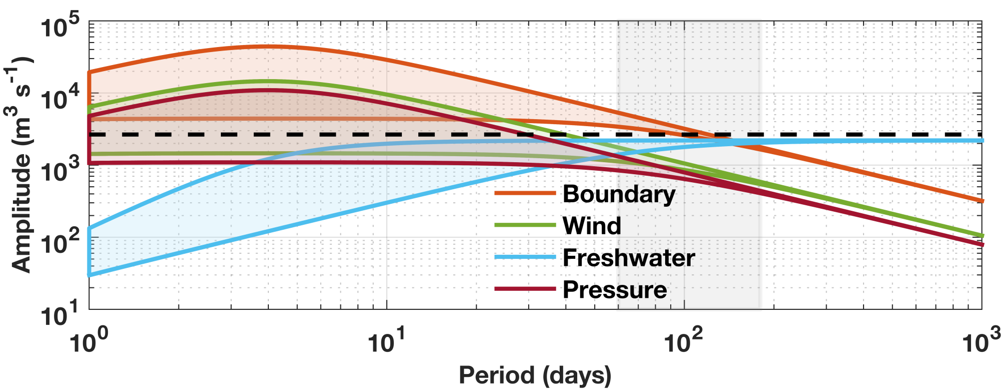


Fig. A1. Amplitude of $vWH$ response to boundary forcing $\zeta_0$ (orange), wind stress $\tau$ (green), freshwater flux $\overline{q}$ (blue), and barometric pressure $\overline{p}$ (red) as a function of period. Values are based on Eqs. (A4), (A6), (A8), (A10) using parameter values from Table 3. Upper and lower lines are bounds determined by the range of friction coefficient $r$. See text for more details. Gray shading indicates intraseasonal periods of primary interest here. Dashed black line is the standard deviation of estimated transport described in the Discussion section.